

Photoluminescence from metal nanostructures - dependence on size

Imon Kalyan,[†] Ieng Wai Un,^{‡,¶} Gilles Rosolen,[§] Nir Shitrit,[†] and Yonatan Sivan^{*,†}

[†]*School of Electrical and Computer Engineering, Ben-Gurion University of the Negev,
Israel*

[‡]*Guangdong Basic Research Center of Excellence for Structure and Fundamental
Interactions of Matter, School of Physics, South China Normal University, Guangzhou
510006, China*

[¶]*Guangdong-Hong Kong Joint Laboratory of Quantum Matter, South China Normal
University, Guangzhou 510006, China*

[§]*Micro and Nanophotonic Materials Group, Research Institute for Materials Science and
Engineering, University of Mons, 7000 Mons, Belgium*

E-mail: sivanon@bgu.ac.il

Abstract

For decades, there have been multiple seemingly contradicting experimental reports on the dependence of the photoluminescence from metal nanostructures on their size. We reconcile these reports using a simple analytic formula which is found to match well photoluminescence measurements for a range of structures and illumination conditions. Our expression requires only knowledge of the local electric field and temperature, and it points to the physical quantities that determine the emission strength and its dependence on size.

1 Introduction

The emission of light from metal nanostructures induced by illumination, frequently referred to colloquially as metal photoluminescence (PL), is a fundamental process occurring in a prototypical solid-state system¹. It also has practical importance - metal nanoparticles are frequently used as non-bleaching fluorescent labels in bio-imaging,^{1,2} correlative light-electron microscopy,³ and more recently, as enablers of thermometry.⁴⁻⁸

Despite that dual importance, it is surprising that many aspects of the metal PL have been under debate for decades. These debates are on, for example, whether the emission occurs due to recombination of an electron and hole residing both within the conduction band⁹⁻¹¹ or involving a hole in the valence band (e.g., Ref. [12-17]), on whether the emission statistics is fermionic or bosonic (e.g., Ref. [6,18]), thermal or non-thermal (e.g., Ref. [10,11,19-21]), or how it depends on the local electric field (e.g., Ref. [10,19,20,22]). Of particular interest is the dependence on the size of the nanostructure (e.g., Ref. [15,16,23-25]). In particular, many early works studied the emission from metal clusters or few nm particles, primarily focussing on atomistic considerations and ligand coverage; these works highlighted the trade-off between the presence of a plasmonic resonance and the quantum yield for emission, see Ref. [26]. For larger structures, there have been reports of contradicting trends. For example, Dulkeith *et al.* Ref. [23] showed that the (time and) frequency integrated Stokes emission (SE) from spheres of growing radii illuminated by a short pulse scales linearly with their volume; similar results were reported by Gaiduk *et al.* Ref. [24] for continuous wave (CW) illumination. On the other hand, Lin *et al.* Ref. [27] and more recently, Bowman *et al.* Ref. [28] have demonstrated that the CW PL from rods and thin Au films, respectively, decreases with growing thickness; similar trends were reported in Ref. [16,29] for pulsed illumination. Other works reported a varying trend (e.g., Ref. [25]).

¹In many cases, the term photoluminescence is used to refer to spontaneous emission / radiative recombination of an electron and a hole, in contrast to inelastic light scattering, aka electronic Raman scattering. In that sense, in this work we use the term photoluminescence (PL) as a shorthand for emission, without distinguishing between these possibilities.

These debates originate from the different conditions under which the PL measurements have been made (in terms of the number, density and shape of the nanostructure geometry, the illumination duration, intensity and wavelength, the relative position of the latter with respect to the resonances of the structure, the relative spectral position of emission with respect to the illumination wavelength, the geometry and thermal properties of the surrounding etc.) or the exact quantity studied, but also from the absence of a simple theory that encompasses both photonic aspects of the problem (via the photonic density of states, as appearing in Purcell's formula), as well as the thermal aspects and the electronic aspects, i.e., the distribution and associated weights of the continuum of possible recombination transitions.

Recently, Dubi and Sivan employed a simple analytic expression for the steady-state electron distribution in a Drude metal to derive an equally simple expression for the PL from metals illuminated by CW light.¹¹ By relying on the empiric values of the permittivity to determine the absorption, this approach circumvents the need to specify the transition matrix element and circumvents the arguments about the origins of the emission (being radiative recombination or electronic Raman / inelastic light scattering etc.^{4,28,30-33}). This expression enabled the resolution of many of the disagreements described above (in particular, associated with the emission statistics and electric-field dependence). This expression was more recently extended to explain the dependence of the PL following short pulse illumination on the electric field.³⁴

In this work, we use the approach of Ref. [11] to reconcile the various seemingly contradicting reports on the size-dependence of the PL from the prototypical geometries of metal particles and layers. Specifically, in Section 2, we combine the analytic expression of Ref. [11] with the detailed analysis of the heating of illuminated metal spheres³⁵ and most importantly, with recent progress made by Loirette-Pelous and Greffet who showed how to determine the total PL of a metal nanostructure in the case of a non-thermal distribution.³⁶

In Section 3, we use the resulting analytic expression to compute the PL from metal

nano-spheres and nano-layers as a function of their size. We distinguish between three cases. For weak illumination (hence, negligible heating), the dependence of the PL spectrum (both the Stokes Emission (SE) and the anti-Stokes Emission (aSE)) on the structure size is determined by a single parameter - the absorption cross-section density (or equivalently, the emission cross-section density). Thus, generically, *the PL scales with the illuminated volume* - it is a volume effect for small sizes and it becomes a surface effect when the size exceeds the light penetration depth. In the latter case, the resonances characteristic of particles modify further the size-dependence of the PL. Indeed, a change of size causes the emission at a given frequency to shift in and out of resonance.

For stronger illumination (hence, moderate heating), the size-dependence of the PL is amplified through the dependence of the Bose function on the (electron) temperature. This has a fairly small effect on the SE, but a large effect on the aSE due to the exponential dependence of the Bose function on the temperature, which itself scales with the absorption cross-section density. For even stronger heating, thermo-optic effects kick in, and cause the quality factor of the resonance to decrease.^{37,38} This causes weaker (excessive) heating at resonance (away from resonance), and hence, has a complex effect on the PL, depending on the emission frequency (SE/aSE).

We then demonstrate a good qualitative match between the prediction of our model and experimental results for spheres and layers, and even good quantitative matches in most cases. We demonstrate different trends by looking also at other particles shapes (rods and nano disks), and find a good qualitative match, even in the presence of modest field and temperature non-uniformity levels. Remarkably, the agreement extends beyond the formal limits of the analysis, specifically, in the presence of interband emission events, which are not accounted for in our analytic expression.

In Section 4, we discuss possible reasons for the occasional quantitative mismatches we observe, the implications of the results, their pros and cons compared with more sophisticated approaches in the literature, specifically, the rigorous momentum-space calculations provides

in Ref. [28,29,32], and mention possible extensions of our approach.

2 Theory

2.1 A microscopic view

In Ref. [11], Sivan and Dubi presented a quantitative theory for the PL from Drude metals under continuous wave (CW) illumination, showing that the *probability* of emitted photons per unit frequency is given approximately by

$$\Gamma^{em}(\mathbf{r}, \omega, \omega_L; \mathcal{E}_F) \cong \gamma_{\mathcal{E}}(\mathbf{r}, \omega, \omega_L; \mathcal{E}_F) \rho_e^2(\mathcal{E}_F) I_e(\omega, \omega_L, |\mathbf{E}_L(\omega_L, \mathbf{r})|^2), \quad (1)$$

where

$$I_e(\omega, \omega_L, |\mathbf{E}_L(\omega_L, \mathbf{r})|^2) = \int f(\mathcal{E} + \hbar\omega, |\mathbf{E}_L(\omega_L, \mathbf{r})|^2) [1 - f(\mathcal{E}, |\mathbf{E}_L(\omega_L, \mathbf{r})|^2)] d\mathcal{E} \quad (2)$$

represents the electronic contribution to the emission formula and

$$\gamma_{\mathcal{E}}(\mathbf{r}, \omega, \omega_L, \mathcal{E}) = \frac{\pi\omega_L V^2}{\epsilon_0} |\vec{\mu}(\mathcal{E}, \mathcal{E} + \hbar\omega_L)|^2 \rho_{phot}(\mathbf{r}, \omega) \quad (3)$$

represents the emission rate of a single electron. In the above, \mathbf{r} and ω are the emitter position vector and frequency, ω_L is the excitation frequency, \mathcal{E}_F is the Fermi energy, ρ_e is the electron density of states and \mathbf{E}_L is the local field. f is the non-equilibrium electron distribution function, $|\vec{\mu}(\mathcal{E}_f, \mathcal{E}_i)|$ is the transition dipole moment between electronic states with an initial energy \mathcal{E}_i and final energy \mathcal{E}_f (assumed to be energy-independent) and $\rho_{phot}(\mathbf{r}, \omega)$ is the local density of photonic states (LDOPS).

Based on the CW solution for f (the steady-state electron distribution) obtained in Ref. [39,40] for uniformly illuminated Drude metals and its experimental verification in Ref. [41–44], the electronic part of the emission formula in Eq. (2) was shown in Ref. [11] to consist

of a series of Planck's black-body radiation-like terms (\mathcal{E}_{BB}), i.e.,

$$\begin{aligned} I_e(\omega, \omega_L, |\mathbf{E}_L(\omega_L, \mathbf{r})|^2) &\sim I_e(\omega, \omega_L, T_e, |\mathbf{E}_L(\omega_L, \mathbf{r})|^2) \\ &\sim \langle \mathcal{E}_{BB}(\omega; T_e) \rangle + 2\langle \mathcal{E}_{BB}(\omega - \omega_L; T_e) \rangle \delta_E + \langle \mathcal{E}_{BB}(\omega - 2\omega_L; T_e) \rangle \delta_E^2 + \dots, \end{aligned} \quad (4)$$

where $\langle \mathcal{E}_{BB}(\omega, T_e) \rangle = \hbar\omega / (e^{\frac{\hbar\omega}{k_B T_e}} - 1)$ and

$$\delta_E(\mathbf{r}; \omega_L, pol', \hat{k}') = p_{abs}(\mathbf{r}; \omega_L, pol', \hat{k}') / p_{sat}. \quad (5)$$

Here, T_e is the electron temperature; for CW illumination, the latter is nearly equal to the phonon temperature, however, since the PL literature is inconsistent on the matter, the notation adopted in this manuscript emphasizes that the dependence is on the electron temperature. Further, the absorbed power density (p_{abs}) is defined in terms of the local $\mathbf{E}_L(\mathbf{r}; \omega_L, pol', \hat{k}')$ as

$$p_{abs}(\mathbf{r}; \omega_L, pol', \hat{k}') = \frac{\omega_L \epsilon_0}{2} \epsilon_m''(\omega_L) |\mathbf{E}_L(\mathbf{r}; \omega_L, pol', \hat{k}')|^2 = \alpha_{abs}(\mathbf{r}; \omega_L, pol', \hat{k}') I_{in}(\mathbf{r}; \omega_L, pol', \hat{k}'), \quad (6)$$

where $\alpha_{abs}(\mathbf{r}; \omega_L, pol', \hat{k}')$ is the absorption cross-section density or, in more general terms, the absorbed power density per unit incident intensity (I_{in}) of polarization pol' and incidence direction \hat{k}' at a position \mathbf{r} corresponding to the illumination frequency. The saturation power density can be approximated by Ref. [11,40]

$$p_{sat}(\omega_L) = \frac{3 n_e (\hbar\omega_L)^2}{4 \mathcal{E}_F \tau_{e-e}}, \quad (7)$$

where n_e is the electron density and τ_{e-e} is an average rate of collisions between electrons. For simplicity, we set τ_{e-e} in Eq. (7) to a value typical for a non-thermal electron, i.e., at $\mathcal{E} \sim \mathcal{E}_F + \hbar\omega$.

The first term in Eq. (4), represents the average energy of thermal emission per electro-

magnetic mode (i.e., for vacuum electric fields); the next terms represent the non-thermal emission induced by deviations of the electron distribution from thermal equilibrium due to one photon absorption (1PA), two photon absorption (2PA) etc.. As discussed in Ref. [11,34], for CW illumination, typically these terms are small compared to the thermal emission at mid-IR frequencies, but dominate the emission close to the illumination frequencies and higher^{11,34} as depicted in the schematic representation (Fig. 1). The complete step structure of the non-thermal contributions was observed experimentally for CW illumination for the first time in Ref. [17].

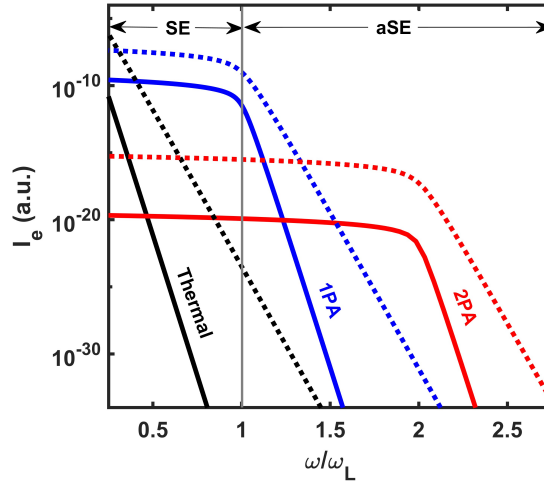


Figure 1: (Color online) Schematic of the contribution from thermal emission: $\langle \mathcal{E}_{BB}(\omega; T_e) \rangle$ (black), 1PA: $2\langle \mathcal{E}_{BB}(\omega - \omega_L; T_e) \rangle \delta_E$ (blue), 2PA: $\langle \mathcal{E}_{BB}(\omega - 2\omega_L; T_e) \rangle \delta_E^2$ (red) from Eq. (4) calculated under CW wave illumination. The plots are shown for two intensities, where solid and dotted lines indicate lower and higher intensities, respectively.

Notably, the emission (1) is assumed to occur strictly within the conduction band, i.e., to involve only intraband transitions. In the presence of interband transitions, this expression can be amended by accounting for the increased number of non-thermal holes above the interband absorption threshold, as shown in Fig. S10(b) of Ref. [28]; as shown below, our analysis provides a qualitative (and usually, also a quantitative) match to the experimental data even without accounting for these additional transitions.

2.2 A macroscopic view

The result (1) applies for a general point within the metal. It was so far used to understand the general parametric dependence of the PL on the electric field, its statistics etc. with only a phenomenological address of the shape and size of the nanostructure.

In order to account for a specific nanostructure geometry, one needs to sum over the random spontaneous emission events from the nanostructure volume as a function of space. This should allow one to account also for the *actual* magnitude of the emission, thus, including also the portion of the emitted photons that got re-absorbed (sometimes referred to as recycled), rather than only the *probability* of emission (as given by Γ^{em} (1)). This can be done using the local Kirchhoff Law for non-isothermal bodies^{45–47} and its extension to metals having non-equilibrium electron distributions.³⁶ The latter study showed that the actual emitted power in the direction \hat{k} into a solid angle $d\Omega$ ($= \frac{d^3k}{k^2 dk}$; see Eq. (9.15.9) in Ref. [48]) is given by

$$dP^{em}(\omega, \omega_L, \hat{k}) \cong \frac{\omega^2}{8\pi^3 c^2} \sum_{pol=s,p} \int_V \alpha_{abs}(\mathbf{r}; \omega, pol, -\hat{k}) I_e(\omega, \omega_L, T_e(\mathbf{r}), |\mathbf{E}_L(\mathbf{r}; \omega_L, pol', \hat{k}')|^2) dr^3 d\Omega, \quad (8)$$

where \hat{k}' is the direction of incidence, pol and pol' are the polarization of the emitted and incident waves, respectively, and $\alpha_{abs}(\mathbf{r}; \omega, pol, -\hat{k})$ is the emission cross-section density (aka emissivity density), which by the local Kirchhoff Law, equals the absorption cross-section density. Unlike in Ref. [36], where the PL was expressed in terms of absorption cross-section, Eq. (8), utilizes the local absorption cross-section density to extend the formulation to structures with nonuniform field distributions, similar to the approach used in Ref. [45–47]. It is notable to mention again that since the formula above accounts only for emission within the conduction band, then, strictly, the emissivity density represented by $\alpha_{abs}(\mathbf{r}; \omega, pol, -\hat{k})$ should include only the intraband contribution to the absorption cross-section density (as

in Ref. [36]). This would not matter for the illustrative examples below, for which we study Ag nanostructures, but could somewhat affect the match between our predictions and the experimental data (see Sections 3.1.5 and 3.2.3).

Using Eqs. (4)-(6) in Eq. (8) gives

$$\begin{aligned}
 dP^{em}(\omega, \omega_L, \hat{k}) \sim & \frac{\omega^2}{8\pi^3 c^2} \sum_{pol=s,p} \int_V \left[\frac{I_{in}}{p_{sat}} \alpha_{abs}(\mathbf{r}; \omega, pol, -\hat{k}) \alpha_{abs}(\mathbf{r}; \omega_L, pol', \hat{k}') \right. \\
 & 2 \langle \mathcal{E}_{BB}(\omega - \omega_L; T_e) \rangle_r + \frac{I_{in}^2}{p_{sat}^2} \alpha_{abs}(\mathbf{r}; \omega, pol, -\hat{k}) \alpha_{abs}^2(\mathbf{r}; \omega_L, pol', \hat{k}') \\
 & \left. \langle \mathcal{E}_{BB}(\omega - 2\omega_L; T_e) \rangle_r + \dots \right] dr^3 d\Omega. \tag{9}
 \end{aligned}$$

Eq. (9) shows that the quantities that determine the emission are the absorption cross-section density α_{abs} and the (electron) temperature distribution. As shown below, the simplified expression (9) also circumvents the more advanced yet complicated k -space calculations (as e.g., in Ref. [28,29,32]), without compromising much predictive capabilities.

We now note that the spatially-integrated emission (9) involves space-varying functions. Specifically, the spatial distribution of α_{abs} depends on the material constituents and geometry of the nanostructure. In addition to gradients induced by illumination non-uniformity (e.g., when a focussed beam illuminates a film), it exhibits significant gradients on scales exceeding the penetration (skin) depth, i.e., for more than a few tens of nm for noble metals. In contrast, the non-uniformity of temperature is typically much weaker than that of the electric field (and hence α_{abs}) due to the strong (electron, hence) heat diffusion in metals. Specifically, the (electron) temperature non-uniformity should, in principle, be extracted from a self-consistent solution of microscopic equations for the electron dynamics; however, in practice, since the deviation from thermal equilibrium is minute for CW illumination,^{39,40,44} it is usually determined by coarse-graining such equations into heat equations, see, e.g., Ref. [39,40,49,50]. Accordingly, the derived single or two temperature models reveal that heat gradients and electron-phonon temperature differences are very small (see,

e.g., Ref. [51–56]). Finally, like the absorption cross-section density α_{abs} and unlike the electron temperature T_e , the non-thermal part of the electron distribution, manifested via δ_E (5), is roughly determined by the local electric field distribution. As predicted in Ref. [30,57,58] and demonstrated experimentally in Ref. [28], the reason for that is the minimal (few nm) mean free path of these electrons, which in turn, originates from their femtosecond-scale collision rate. Accordingly, in what follows we will use heat equations to determine the electron temperature and rely on the solution of Maxwell’s equations to determine the electric field, and hence, the spatial distribution of α_{abs} and δ_E . Having said that, in many cases (specifically, for few nm spheres and uniformly illuminated thin films, both studied below), α_{abs} is quite uniform. In such cases, α_{abs} can be estimated from measurable quantities like the absorption cross-section, σ_{abs} (in the case of particles) or absorptance, A (in the case of films), thus, simplifying the formulation slightly, and making the analysis of the PL simpler.

3 Results

3.1 Nano-spheres under CW illumination

3.1.1 Determination of the electron temperature

We start our analysis by considering the PL from nano-spheres under CW plane wave illumination in a uniform optical and thermal environment (oil, in our case), see Fig. 2(a). We choose silver as a prototypical plasmonic material, as it does not require accounting for interband transitions for illumination with visible light. As mentioned above, in this case, it is customary to neglect the small difference between the electron and phonon temperatures (see, e.g., Ref. [39,40,59]) and consider a single temperature model. Nevertheless, as mentioned, we choose to denote the temperature below as T_e , in order to emphasize that it is the electron temperature that is the relevant quantity as far as photon emission is concerned. Then, the steady-state temperature $T_e(\mathbf{r})$ can be obtained by solving the heat

diffusion equation⁶⁰

$$\nabla \cdot [\kappa(\mathbf{r})\nabla T_e(\mathbf{r}, \omega_L)] = \begin{cases} -\alpha_{abs}(\mathbf{r}; \omega_L)I_{in}, & \text{inside the nanostructure,} \\ 0, & \text{outside the nano structure,} \end{cases} \quad (10)$$

where κ is the thermal conductivity and we used Eqs. (6) on the right-hand-side. Due to the symmetry, $\alpha_{abs}(\mathbf{r}; \omega_L)$ for a nanosphere is independent of the direction and polarization of the incident beam.

As shown already in Ref. [35,60], even in the presence of substantial field non-uniformity (occurring for nano-spheres of more than a few tens of nm in size), the high thermal conductivity of the metal ensures that the temperature of the nanosphere is only weakly inhomogeneous. In fact, as shown in Ref. [35], the temperature can be calculated quite accurately also when replacing $\alpha_{abs}(\mathbf{r}; \omega_L)$ in Eq. (10) by its spatial average, $\langle \alpha_{abs}(\mathbf{r}; \omega_L) \rangle_r = \frac{1}{V} \int \alpha_{abs}(\mathbf{r}; \omega_L) d\mathbf{r} = \sigma_{abs}(\omega_L)/V$. Particularly, for spheres whose radius is up to ≈ 60 nm, the temperature can be approximated as

$$T_e \approx \langle T_e \rangle_r = T_h + \frac{\langle \alpha_{abs}(\mathbf{r}; \omega_L) \rangle_r I_{in}}{3\kappa_h} a^2. \quad (11)$$

Here, κ_h and T_h are the thermal conductivity and the temperature of the surrounding media far from the particle.

As a representative example, Fig. 2(b)-(c) show $\langle \alpha_{abs}(\mathbf{r}; \omega_L) \rangle_r$ and the (electron) temperature (11), respectively, calculated for Ag spheres of sizes up to 60 nm dispersed in oil (permittivity $\epsilon_h = 2.235$, thermal conductivity $k_h = 0.2873 \text{ Wm}^{-1}\text{K}^{-1}$) for an excitation laser wavelength λ_L close to the (dipolar) plasmon resonance (488 nm) and for a wavelength farther from the resonance (900 nm). The absorption cross-section (density) is well studied,⁶¹ hence, described below only briefly. Specifically, $\langle \alpha_{abs}(\mathbf{r}; \lambda_L = 488\text{nm}) \rangle_r$ shows a peak around 30 nm. For $a < 10$ nm, the absorption cross-section $\sigma_{abs}(\omega_L)$ (hence, $\langle \alpha_{abs}(\mathbf{r}; \omega_L) \rangle_r \sim \sigma_{abs}(\omega_L)/a^3$) takes the quasi-static form, $\sigma_{abs}^{qs} \simeq \frac{6\pi}{\lambda} V \Im \left(\frac{\epsilon - \epsilon_{bg}}{\epsilon + 2\epsilon_{bg}} \right)$ (see Fig. 9

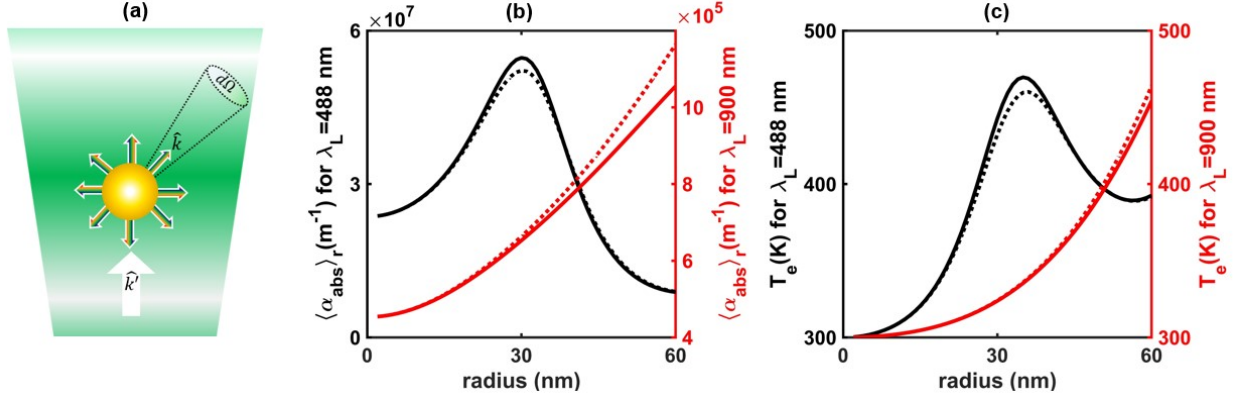


Figure 2: (Color online) (a) A schematic illustration of light emission from a sphere. (b) The absorption cross-section density $\langle \alpha_{abs} \rangle_r$ vs. radius for $\lambda_L = 488$ nm (black) and 900 nm (red) for Ag spheres in oil. (b) The corresponding (electron) temperature reached due to CW illumination of the Ag spheres, calculated using Eq. (11). The corresponding illumination intensities are $I_{in} = 0.25$ MW/cm² (black line) and $I_{in} = 3.5$ MW/cm² (red line). The thermo-optic effect on $\langle \alpha_{abs} \rangle_r$ and T_e is represented by the dotted lines.

or more generally, Ref. [61]). As the sphere radius increases, the $\lambda \sim 400$ nm dipole resonance undergoes a red-shift (see Fig. 10(a)). Thus, since the chosen excitation wavelength $\lambda_L \sim 488$ nm is at the long wavelength tail of the resonance, $\langle \alpha_{abs}(\mathbf{r}; \omega_L) \rangle_r$ increases with a as the dipole resonance tunes towards λ_L . However, the strength of the dipole resonance decreases with growing sphere size, so that beyond $a \sim 30$ nm, the absorption becomes limited to the surface as the importance of higher-order resonances increases. The corresponding size dependence of σ_{abs} is shown in Fig. 9.

For excitation at $\lambda_L = 900$ nm, the averaged absorption cross-section density $\langle \alpha_{abs} \rangle_r$ increases monotonically with the sphere size and its peak occurs beyond the range of consideration in this work, see Fig. 9(b). In that sense, the off-resonance illumination case behaves as in the small size regime of the on-resonance case; we will not dwell on it further in this study.

Fig. 2(c) shows the corresponding size-dependence of the electron temperature. By Eq. (11), and as explained in Ref. [35], the size-dependence of the temperature T_e originates from the proportionality with $\langle \alpha_{abs}(\mathbf{r}; \omega_L) \rangle_r$ and a^2 . Specifically, for on-resonance excitation, the product $\langle \alpha_{abs}(\mathbf{r}; \omega_L) \rangle_r a^2$ results in a peak of T_e at ≈ 35 nm while for off-resonance ex-

citation, the monotonic increase of $\langle \alpha_{abs}(\mathbf{r}; \omega_L) \rangle_r$ results in a monotonic increase of T_e . The similarity to the size-dependence of the absorption cross-section density is apparent.

3.1.2 Determination of the PL

Fig. 3 illustrates the size-dependence of the total PL (as per Eq. (9)) for an excitation wavelength close to resonance ($\lambda_L = 488$ nm). The intensities used for the calculations are chosen such that at the lower intensity ($I_{in} = 2.5 kW/cm^2$), the temperature of each sphere is close to room temperature and at the higher intensity ($I_{in} = 0.25 MW/cm^2$) the maximum temperature does not exceed $500^\circ K$ (for which sintering and damage may start to occur). The calculations are conducted at three different emission wavelengths. The calculated emission at $\lambda = 420$ nm (aSE; Fig. 3(a)) displays a peak at $a = 28$ nm when excited by the low intensity. When excited at a higher intensity (Fig. 3(d)), the peak slightly red-shifts to $a = 34$ nm and becomes more distinct. For the emission at $\lambda = 680$ nm (SE; Fig. 3(b) and (e)), the PL increases monotonously until $a \approx 42$ nm, decreases until $a = 51$ nm and then rises again. The PL at $\lambda = 950$ nm, (lower frequency SE; Fig. 3(c) and (f)) exhibits a similar behavior, except for a higher slope beyond $a = 50$ nm.

As already noted above, the expression for PL (9) can be further simplified for a sphere. As discussed in Section 3.1.1, the temperature is fairly uniform in the sphere and the space-dependence of I_e in Eq. (9) originates only from that of δ_E , as indicated by Eq. (4). Further, we rely on the calculations of the mean free path of the non-thermal electrons³⁰ to justify the neglect of spatial broadening of the non-thermal electron distribution. These results motivate the use of the analytic result (4) also for non-uniform fields, i.e., to approximate the level of non-thermal electron population δ_E by simply summing over its local value across the particle volume. Accordingly, δ_E (5) can be expressed in terms of the spatially averaged, $\langle \alpha_{abs}(\mathbf{r}; \omega_L) \rangle_r$. With this consideration, I_e (4) becomes independent of position. The volume integration over $\alpha_{abs}(\mathbf{r}; \omega)$ is now replaceable by the absorption cross-section of the sphere,

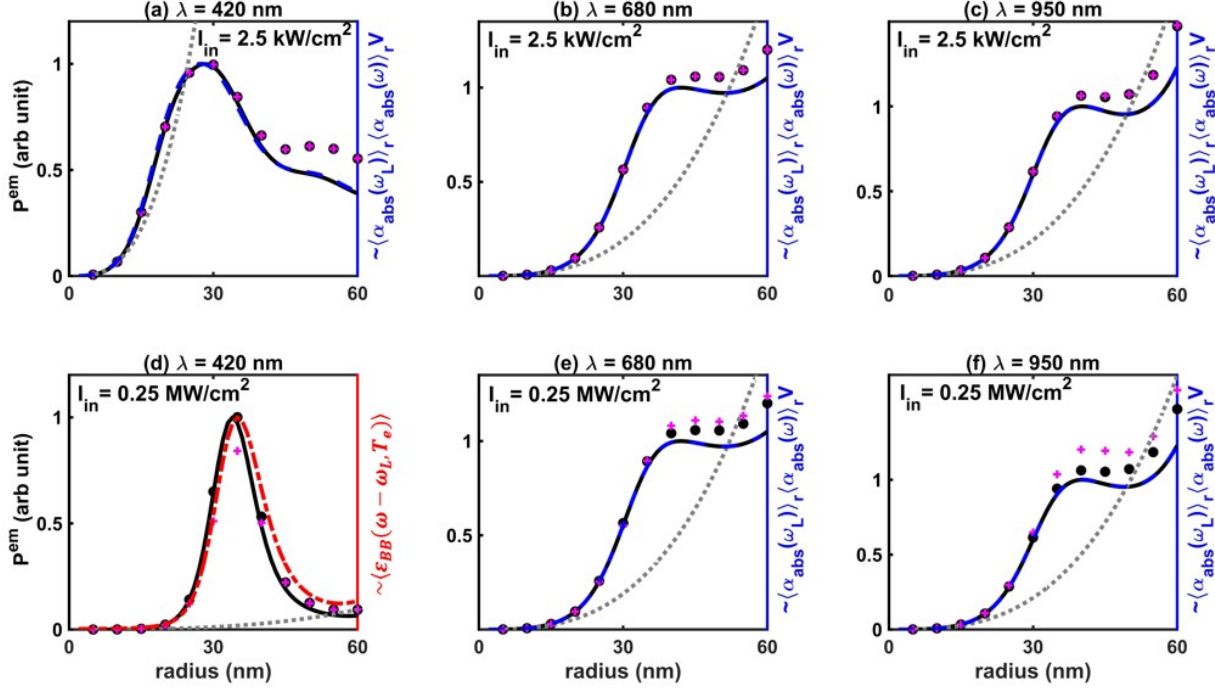


Figure 3: (Color online) The total PL (Eq. (9); circles) and its homogenized approximation (Eq. (12); black continuous line) calculated for spheres under CW illumination with $\lambda_L = 488$ nm and emission wavelengths of $\lambda = 420$ nm ((a) and (d)), $\lambda = 680$ nm ((b) and (e)) and $\lambda = 950$ nm ((c) and (f)). For these calculations, $p_{sat} \sim 1.2 \times 10^{25}$ W/m³ and I_{in} used for the calculation are (a)-(c) 2.5 KW/cm² and (d)-(f) 0.25 MW/cm². The magenta crosses show the PL calculation when the thermo-optic effect is included. The dashed blue lines represent $a^3 \langle \alpha_{abs}(\lambda_L) \rangle_r \langle \alpha_{abs}(\lambda) \rangle_r$ and the red dash-dot lines represent $\langle \mathcal{E}_{BB} \rangle$. The gray dotted lines are an a^3 fit to the calculation for $a < 10$ nm. Frequency and wavelength are used interchangeably, as convenient.

which in turn, can be expressed as $\sigma_{abs}(\omega) \sim a^3 \langle \alpha_{abs}(\mathbf{r}; \omega) \rangle_r$. Thus, Eq. (9) simplifies to

$$dP^{em}(\omega, \omega_L) \sim \omega^2 a^3 \langle \alpha_{abs}(\mathbf{r}; \omega) \rangle_r \left[2 \frac{I_{in}}{p_{sat}(\omega_L)} \langle \alpha_{abs}(\mathbf{r}; \omega_L) \rangle_r \langle \mathcal{E}_{BB}(\omega - \omega_L; T_e) \rangle_r + \left(\frac{I_{in}}{p_{sat}(\omega_L)} \right)^2 \langle \alpha_{abs}(\mathbf{r}; \omega_L) \rangle_r^2 \langle \mathcal{E}_{BB}(\omega - 2\omega_L; T_e) \rangle_r \right] d\Omega. \quad (12)$$

Using this expression, we can determine the total PL solely via the absorption cross-section density evaluated at the pump frequency ($\langle \alpha_{abs}(\mathbf{r}; \omega_L) \rangle_r$, Fig. 2(b)) and emission frequency ($\langle \alpha_{abs}(\mathbf{r}; \omega) \rangle_r$, Fig. 10(a)), as well as the electron temperature (Fig. 2(c)). As seen in Fig. 3(a)-(c), the qualitative behaviour of the PL (Eq. (9)) and its approximation (Eq. (12)) is nearly identical except for the former being slightly higher for $a > 30$ nm.

While the computational simplification associated with Eq. (12) is minor, its more significant contribution is to allow us to pinpoint the origins of the behaviour observed in Fig. 3. Specifically, the PL in Fig. 3(a)-(c) pertains roughly to room temperature for all sphere sizes making the Bose function ($\mathcal{E}_{BB}(\omega - \omega_L)$) essentially size-independent. In this scenario, the PL varies with sphere size as the product of $\langle \alpha_{abs}(\mathbf{r}; \omega_L) \rangle_r$ (at the absorption wavelength), $\langle \alpha_{abs}(\mathbf{r}; \omega) \rangle_r$ (at the emission wavelength) and the volume, V . For spheres of radius $a < 10$ nm (i.e., safely within the quasi-static regime), $\langle \alpha_{abs} \rangle_r$ has a very weak dependence on the volume (see Fig. 9) so that the PL scales as a^3 . For larger spheres, the sub-volume scaling of the absorption and temperature, along with variations in $\langle \alpha_{abs} \rangle_r$ with particle size owing to the sphere's modal response (see Ref. [35] and Fig. 2(b)) result in the observed deviation from the volume scaling, namely, the peaks and troughs in the PL shown in all subplots of Fig. 3. Specifically, the non-monotonic behaviour in the PL observed for the larger sizes are due to the combined effect of the system tuning into and then out of the dipole resonance, and then tuning into the quadrupole mode. In that respect, considering the PL as being a volume effect for small spheres, and as a surface effect for larger spheres, is a crude description, which misses the dominant effect of the modal structure.

Fig. 3(d)-(f) shows the PL for a higher intensity which results in a size-dependent temper-

ature, varying from room temperature to $\sim 500^\circ K$ (see Fig. 2(c)). The higher and varying temperature affects differently the different parts of the PL spectrum. First, it hardly affects the SE (Fig. 3(e)-(f)) which thus follows the same trend observed for the low-intensities, at least up to temperatures for which thermo-optic effects are still negligible^{38,62} (see Section 3.1.3). Indeed, for SE, the non-thermal contribution from the 1PA term dominates I_e (see Eq. (4), Fig. 1 and Fig. 11), which is nearly temperature-independent since it originates from the non-thermal electron shoulders given in Eq. (5) (see SI Section S3 of Ref. [11]). In contrast, the aSE is exponentially sensitive to the temperature via the Bose function $\langle \mathcal{E}_{BB}(\omega - \omega_L; T_e) \rangle$ (see Fig. 1). As a result, the size-dependence of the PL is much stronger (see Fig. 3(d)), exhibiting superlinear scaling with the volume.

Deeper into the aSE regime, the 2PA term becomes stronger than the 1PA term, see Fig. 1. To demonstrate this, we calculate the PL for a longer (off-resonant) excitation wavelength (900 nm, i.e., smaller ω_L), see Fig. 12. In this case, while the near aSE (Fig. 12(b) and (f)) grows as $\langle \alpha_{abs}(\mathbf{r}; \omega_L) \rangle_r$, for frequencies sufficiently deep into the aSE, the PL scales as $\sim \langle \alpha_{abs}(\mathbf{r}; \omega_L) \rangle_r^2$ at low intensity excitation (Fig. 12(a)) and as $\sim \langle \mathcal{E}_{BB}(\omega - 2\omega_L) \rangle$ at high intensity illumination (Fig. 12(d)).

Finally, in order to show the generality of our approach, and to demonstrate that the behaviour we identify is not qualitatively affected by the choice of the exciting laser frequency (e.g., its position with respect to resonance), we replicate the results of Fig. 3 (for which the illumination is on the red-side of the plasmon resonance) in Fig. 13 and Fig. 14 for backgrounds with higher refractive indices. This results in a red-shift of the resonances and introduces the higher-order modal response to the PL emission, particularly, for the larger spheres. However, the qualitative behaviour is similar to that with the lower background refractive index.

3.1.3 The thermo-optic effect

Illumination at high intensity can induce significant changes in the temperature of the spheres, consequently altering their permittivity via the so-called thermo-optic effect,^{37,63,64} and as a result, modify the absorptivity (hence, the emissivity) and finally the PL. To analyze this effect, we assume that the permittivity of the metal and the thermal conductivity of the surrounding medium depend linearly on the change of temperature, compute the thermo-derivative of the metal permittivity from ellipsometry data⁶⁵ and set the thermo-derivative of the thermal conductivity of the surrounding medium to $1.3 \times 10^{-4} \text{ Wm}^{-1}\text{K}^{-2}$, as in Ref. [62]; the temperature of the nanoparticle is then calculated using the method described by Un *et al.*⁶²

Overall, as the intensity (hence, temperature) increases, the real part of the permittivity (ϵ'_m) becomes more negative, while the imaginary part (ϵ''_m) increases to higher positive values at most frequencies. This results in a blue shift of the resonance peak and a broadening of its spectral width, leading to enhanced absorption at off-resonance frequencies, see Fig. 15 and Ref. [37,64–67]. As a result, $\langle \alpha_{abs}(\mathbf{r}; \omega) \rangle_r$ slightly decreases at 488 nm and slightly increases at 900 nm, as seen in Fig. 2(a). The decrease in the former case leads to a reduction in the temperature for the hottest spheres (around $a = 30$ nm), and hence, to the reduction of the aSE observed in Fig. 3(d). However, the SE PL is hardly affected by the temperature. Thus, the increase in $\langle \alpha_{abs}(\mathbf{r}; \omega) \rangle_r$ at longer wavelengths results in a slight increase of the PL, as observed in Fig. 3(e) and (f). For excitation at 900 nm, the temperature of the spheres (especially for $a > 30$ nm) increases slightly compared to the value calculated for the linear case, leading to a slight increase in the PL for aSE, as shown in Fig. 12(d)-(e). The thermo-optic increase of $\langle \alpha_{abs}(\mathbf{r}; \omega_L) \rangle_r$ and $\langle \alpha_{abs}(\mathbf{r}; \omega) \rangle_r$ leads to a slight increase in SE, as observed in Fig. 12(f).

3.1.4 The quantum size effect

It is well known that the imaginary part of metal permittivities are found to be higher when the dimension of the metal structures falls below 10-20 nm.⁶⁸ This effect is usually modelled by inserting a correction to the collision rate appearing in the Drude permittivity which grows inversely with the structure size.⁶⁹ In that respect, the effect of the small size on the PL is similar to that of the thermo-optic effect, but is limited mostly to the small particle sizes, for which the PL is anyhow weaker. For this reason, we do not show a specific numeric example of this effect for spheres.

3.1.5 Comparison to single particle experiments

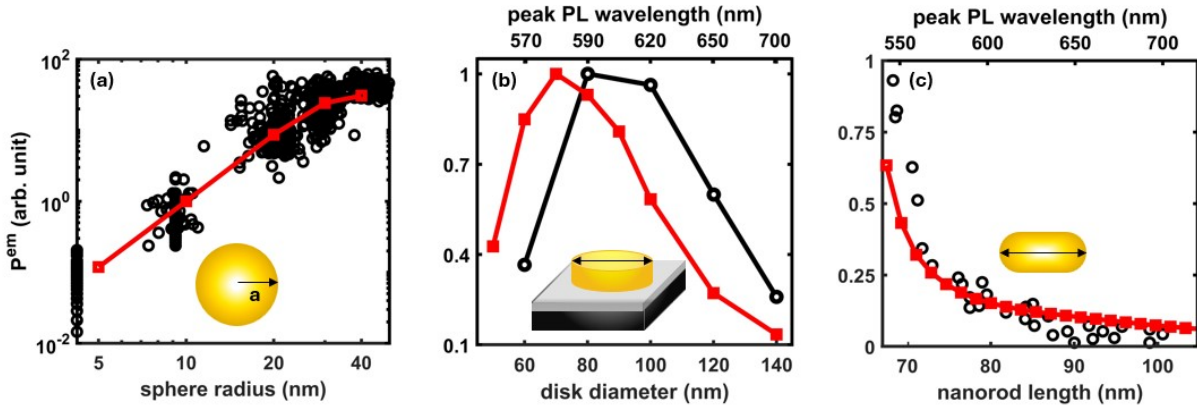


Figure 4: (Color online) (a) Normalized PL from gold spheres on a glass substrate immersed in glycerol with $\lambda_L = 514$ nm with emission integrated over the range of 560 – 640 nm, as measured by Gaiduk *et al.*²⁴. (b) PL peak intensities vs. diameter of gold disks of height 30nm at $\lambda_L = 532$ nm as measured by Hu *et al.*²⁵. (c) Spectrally-integrated PL from silver nanorods of diameter 23 nm on a quartz substrate, at $\lambda_L = 532$ nm as measured by Lin *et al.*²⁷. In all panels, experimental results and theoretical calculations using Eq. (9) are depicted by black circles and red squares, respectively, with corresponding solid lines added for visual guidance. The corresponding calculated PL peak positions are indicated on the top axis of (b) and (c).

Our theoretical predictions can be compared to various single particle PL measurements. First, Fig. 4(a) shows that our calculations align with the experimental observations of the normalized SE PL (spectrally integrated over the range of 560 nm to 640 nm) measured from single gold nanospheres of different sizes, as reported by Gaiduk *et al.* (see Fig. S5 of Ref. [

24]). The illumination intensity was adjusted to keep the temperature rise relatively low (approximately below 20 K). The PL is calculated using Eq. (9) with the refractive index of gold obtained from Ref. [70], and those of glass and glycerol being 1.45 and 1.47, respectively. The normalized PL roughly scales with the volume until $a \sim 30$ nm, but seems to saturate upon further increase in size, in line with our prediction.

Size-dependence of the PL from larger particles was studied by Hu *et al.*²⁵ who demonstrated that the spectral peak of the PL from gold nano-disks on a SiO₂-coated absorptive (silicon) substrate initially increases, reaches a maximum, and then decreases significantly with further increases in size. The absorption cross-section densities and the T_e of the disks are calculated using COMSOL, considering normal incidence and emission perpendicular to the substrate, with the permittivity data for gold and Si taken from Ref. [70] and Ref. [71], respectively. Calculations based on Eq. (9) exhibit a qualitatively similar trend (even if at a slight spectral shift).

Lastly, our theoretical prediction of PL are compared with the PL measurements by Lin *et al.*²⁷ This work showed the spectrally-integrated PL from single nanorods of different lengths with constant diameter along their main axis. In contrast to the nanospheres (and in similarity to layers, shown later), the PL monotonically decreases with nanorod length. These results are reproduced in Fig. 4(c) along with the theoretical prediction, i.e., the spectral integration of Eq. (9). The optical response is calculated in COMSOL, where the substrate refractive index is $n = 1.45$ and the permittivity of the silver rods is taken from Ref. [70]. The temperature is estimated with an approximate expression⁶⁰ and remains close to the ambient temperature (0.1% variation) for the laser illumination intensity considered ($I_{in} = 3$ mW/cm²). Good qualitative agreement is obtained for nanorods longer than 72 nm, however, our prediction underestimates the PL for shorter nanorods, thus providing only a qualitative match for this regime (specifically, in a 30 nm wide wavelength range close to the pump). A similar observation was recently reported above the pump wavelength,³⁶ necessitating a phenomenological adjustment of the theoretical prediction.

Remarkably, while our theory (9) includes only emission events occurring in the conduction band, it successfully predicts the dependence of the emission on the particle size even in spectral regimes where interband emission events should occur (specifically, for the spheres and nano-disks (Fig. 4(a)-(b), respectively). This implies that, in these cases, interband transitions modify the emission features in a modest quantitative manner, but not qualitatively. We expect that inclusion of such transitions may yield a better quantitative match to the experimental results.

3.2 Layers under continuous illumination

We now turn to study the PL from a thin layer of a Drude metal using the approach used for the spheres. Specifically, we examine a thin silver layer on a glass substrate illuminated at normal incidence (hence, no dependence on polarization pol' , and $k_z = |\mathbf{k}'|$, where k_z is the component of \mathbf{k} normal to the surface of the layer) by a focused Gaussian CW beam with an intensity profile $I_{in}(\rho, \omega_L) = I_0 e^{-2\rho^2/b^2}$ as depicted in Fig. 5(a).

3.2.1 Determination of the electron temperature

The absorbed power density and temperature distribution calculated by solving the heat equation (10) using the electromagnetic heat module of COMSOL Multiphysics, are presented in Figs. 5(b)-(c), respectively. The absorbed power density decreases exponentially along the illumination direction (z -axis) due to the short penetration depth (Fig. 5(d)). However, along the radius it exhibits nearly the same distribution as that of the incident intensity, as shown in Fig. 5(e).

In contrast, the temperature variation across the film's thickness is minimal (see Fig. 5(d)) due to the high thermal conductivity of the metal; for the same reason, along the radius, the temperature shows a Gaussian profile with a full width at half maximum (FWHM) greater than that of the incident beam, as illustrated in Fig. 5(e).

Generically, $\alpha_{abs}(\mathbf{r}; \omega_L, pol', \hat{k}')$ is uniform in the plane of the film (i.e., it is independent of

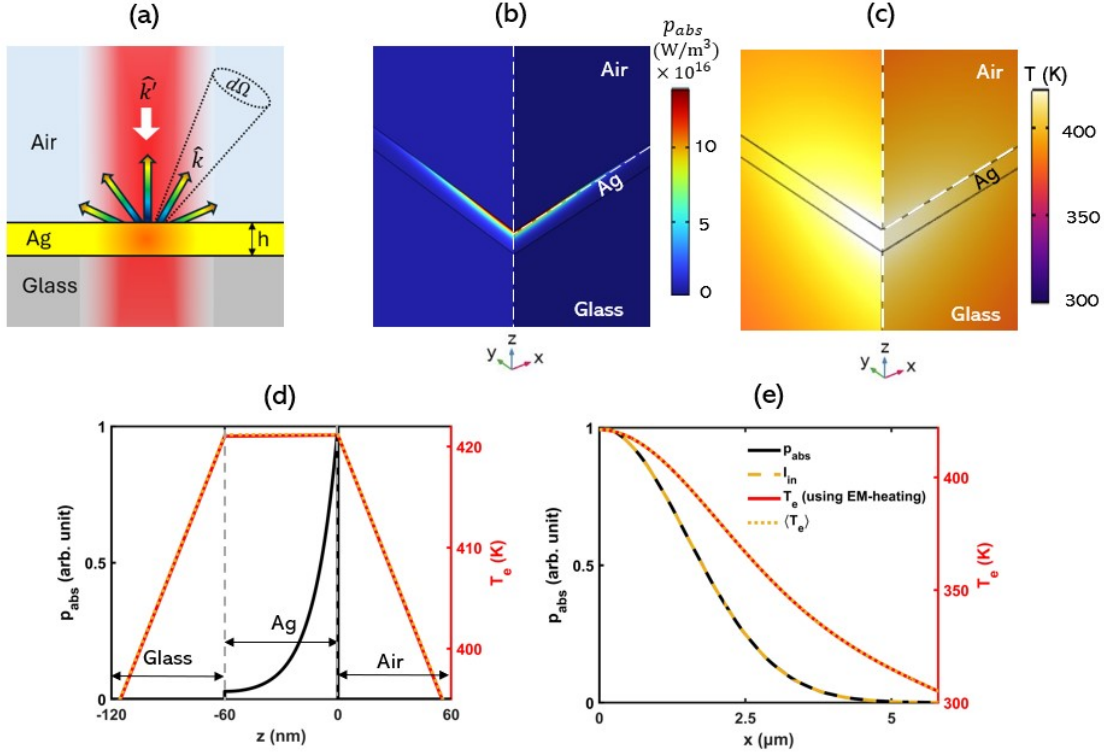


Figure 5: (Color online) (a) Schematic illustration of the emission from an Ag film on a glass substrate illuminated from below by a focused Gaussian beam. (b) The absorbed power density calculated for a 60 nm film due to continuous wave illumination using the electromagnetic heating module of COMSOL Multiphysics (shown on a quarter domain). (c) The corresponding calculated temperature distribution. (d) Vertical (along the z -axis) and (e) transverse (x -axis, $z = 0$) cross-sections of the absorbed power density and temperature. The red-solid and yellow dotted lines in (d) and (e) represent T_e calculated using Eq. (10), considering the actual distribution of $\alpha_{abs}(\mathbf{r}; \omega_L)$ and the position averaged $\langle \alpha_{abs}(\mathbf{r}; \omega_L) \rangle_z$ respectively. The yellow dashed line in (e) represents the distribution of the incident intensity along the x -axis. The peak intensity and radius of illumination are 2 MW/cm² and 3 μ m, respectively.

ρ and ϕ) and varies only along the thickness of the film (i.e., it is only z -dependent). The average value of $\alpha_{abs}(z, \omega_L, pol', \hat{k}')$ along the thickness can be derived from the experimentally measurable quantity, the absorptance $A(\omega, pol', \hat{k}')$ as

$$\langle \alpha_{abs}(z, \omega_L, pol', \hat{k}') \rangle_z = \frac{1}{h} \int_h \alpha_{abs}(z, \omega_L, pol', \hat{k}') dz = \frac{A(\omega_L, pol', \hat{k}')}{h}. \quad (13)$$

$\alpha_{abs}(\mathbf{r}; \omega_L, pol', \hat{k}')$ and its average can be calculated using the transfer matrix method.⁷² For normal incidence, this quantity is independent of polarization.

Since the variation of temperature along the film thickness is negligible (see Figs. 5(c)-(d)), the temperature of the film can be calculated by using the z -averaged cross-section density $\langle \alpha_{abs}(z, \omega_L, pol', \hat{k}') \rangle_z$ in Eq. (10). The temperature calculated for a 60 nm Ag film with this approximation closely matches the temperature calculated based on the exact absorbed power density distribution, as shown in Fig. 5(e). This also enables simplifying the expression for the PL in Eq. (9) by separating the integrations with respect to z and ρ , as discussed in more detail in Section 3.2.2.

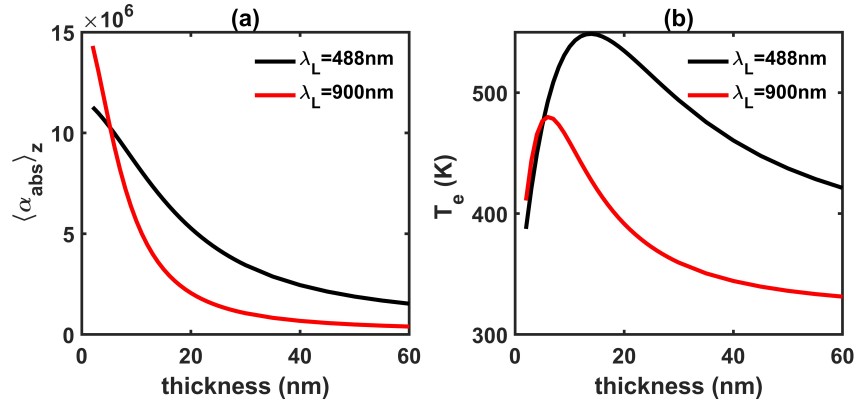


Figure 6: (Color online) (a) $\langle \alpha_{abs} \rangle_z$ and (b) the (electron) temperature of Ag films at the center of the illumination by a CW Gaussian beam with central intensity $I_0 = 2$ MW/cm² and $b = 3\mu\text{m}$, with $\lambda_L = 488$ nm (black) and $\lambda_L = 900$ nm (red).

The size-dependence of $\langle \alpha_{abs}(z; \omega_L) \rangle_z$ for normal incidence at $\lambda_L = 488$ nm and 900 nm are shown in Fig. 6(a). $\langle \alpha_{abs}(z, \omega_L) \rangle_z$ decreases with increasing film thickness for both wavelengths, with this decay occurring more rapidly at the longer wavelength. This trend

can be explained by the distribution of the electric field within the metal film. Typically, the electric field is strongest near the surface of the metal film and exhibits an exponential decay as it penetrates deeper into the material. Thus, as the film thickness increases, the average field, hence, absorptance density A/h decreases. This decay is more rapid for $\lambda = 900$ nm due to its shorter penetration depth ($= 21$ nm) compared to the penetration depth of 26 nm at $\lambda_L = 488$ nm as shown in Fig. 6 and Fig. 10(b).

Unlike the case of spheres, the size-dependence of the film temperature differs from α_{abs} . The temperature at the center of the illumination spot ($\rho = 0$) as a function of film thickness is depicted in Fig. 6(b). Maximal temperature is reached at $h = 14$ nm and 6 nm, corresponding to the short and long wavelengths, respectively. This peak temperature can be explained from Fourier's law of heat transfer (solution of the divergence in Eq. (10)), according to which, $T_e \propto h \langle \alpha_{abs}(z; \omega_L) \rangle_z^2$. Thus, with increasing thickness, the temperature initially increases. However, due to the sharp decline of $\langle \alpha_{abs}(\mathbf{r}; \omega_L) \rangle_r$, with thickness, the temperature eventually decreases, resulting in a peak.

3.2.2 Determination of the PL

Fig. 7 presents the predicted PL obtained using Eq. (9) for Ag films of thickness ranging from 2 nm to 60 nm. For this calculation, we consider normal illumination at a wavelength of 488 nm, with the emitted PL collected within a solid angle $d\Omega$ positioned directly above the illumination point. Calculations are performed at two incident intensities: one for which the films remain roughly at room temperature ($I_0 = 2$ kW/cm²) and the other to elevate their temperature to 550K ($I_0 = 2$ MW/cm²) as shown in Fig. 6(b). At room temperature, the PL at the three emission wavelengths (420 nm, 680 nm and 950 nm) shows peaks at film thicknesses of 13 nm, 8 nm and 6 nm, respectively. Similar to the case of the spheres, when the peak illumination intensity is increased to $I_0 = 2$ MW/cm², the trends of SE remain

²Solving the divergence in Eq. (10) simply along z-axis, we obtain $-\kappa \nabla T_e(z, \rho = 0) \sim h \langle \alpha_{abs}(z; \omega_L) \rangle_z I_{in}(\rho = 0; \omega_L)$. Since the temperature inside the film remains nearly constant along z-axis, and decreases linearly to T_h at a distance Δz outside the film, $T_e(z, \rho = 0) - T_h \sim \frac{\Delta z}{\kappa} h \langle \alpha_{abs}(z; \omega_L) \rangle_z I_{in}(\rho = 0; \omega_L)$.

unchanged so that Figs. 7(e)-(f) are hardly distinguishable from Figs. 7(b)-(c). However, the peak corresponding to aSE becomes narrower.

Similar to the analysis of the PL from particles above, the PL can be again approximated by replacing $\alpha_{abs}(z, \omega_i)$ by its average value along the thickness, $\langle \alpha_{abs}(z, \omega_i) \rangle_z$ as

$$\begin{aligned}
dP^{em}(\omega, \omega_L, \hat{k}) \sim & \sum_{pol=s,p} \frac{\omega^2}{4\pi^2 c^2} \left[\frac{1}{p_{sat}(\omega_L)} \left(h \langle \alpha_{abs}(z, \omega_L) \rangle_z \langle \alpha_{abs}(z, \omega) \rangle_z \right. \right. \\
& \int_{\rho=0}^{\infty} 2I_{in}(\rho, \omega_L) \langle \mathcal{E}_{BB}(\omega - \omega_L; T_e(\rho)) \rangle_z \rho d\rho \Big) \\
& + \frac{1}{p_{sat}^2(\omega_L)} \left(h \langle \alpha_{abs}^2(z, \omega_L) \rangle_z \langle \alpha_{abs}(z, \omega) \rangle_z \right. \\
& \left. \left. \int_{\rho=0}^{\infty} I_{in}^2(\rho, \omega_L) \langle \mathcal{E}_{BB}(\omega - 2\omega_L; T_e(\rho)) \rangle_z \rho d\rho \right) \right] d\Omega.
\end{aligned} \tag{14}$$

Again, the calculations (14) closely match the results with the exact calculations (Eq. (9)), with the SE (Fig. 7(b)-(c),(e)-(f)) and low temperature aSE (Fig. 7(a)) being well approximated by $\langle \alpha_{abs}(z, \omega_L) \rangle_z \langle \alpha_{abs}(z, \omega) \rangle_z h$ for films up to $h \sim 20$ nm, after which the approximation falls below the exact results³. Due to the multiplication by the increasing h and the sharply decreasing $\langle \alpha_{abs}(z, \omega_i) \rangle_z$ (Fig. 6(a)), a peak appears in the PL. The stronger decay of $\langle \alpha_{abs}(z, \omega_i) \rangle_z$ at longer wavelengths causes these peaks to shift slightly towards smaller values of h . However, at the higher temperatures, the aSE undergoes exponential amplification via the $\langle \mathcal{E}_{BB}(\omega - \omega_L; T_e(\rho)) \rangle_z$ term, resulting in the sharper peak compared to that at the room temperature as illustrated in Fig. 7(d).

The PL calculated at the longer excitation wavelength of 900 nm allows us to explore the PL behaviour deeper into the aSE regime, where the 2PA contribution takes over the 1PA contribution, see Figs. 16(a) and (d). For this excitation, while the PL in the near aSE region, (Fig. 16(b) and (e)) can be explained using the same reasoning applied to $\lambda_L = 488$ nm illustrated in Fig. 7(a) and (d), in the deeper aSE regime, the PL varies as $\sim \langle \alpha_{abs}(z, \omega_L) \rangle_z^2$ (rather than $\langle \alpha_{abs}(z, \omega_L) \rangle_z$ at room temperature and as $\sim \langle \mathcal{E}_{BB}(\omega - 2\omega_L, T_e(\rho)) \rangle_z$ (rather

³For films thicker than 30 nm, the PL calculated with Eq. (14) is less than that calculated with Eq. (9) as $\frac{\int_0^h \alpha_{abs}(z, \omega_L) \alpha_{abs}(z, \omega) dz}{h \langle \alpha_{abs}(z, \omega_L) \rangle_z \langle \alpha_{abs}(z, \omega) \rangle_z} \sim \frac{2n''(\omega)k(\omega)n''(\omega_L)k(\omega_L)}{n''(\omega)k(\omega)+n''(\omega_L)k(\omega_L)} > 1$ for $n'' > 1$.

than $\langle \mathcal{E}_{BB}(\omega - \omega_L, T_e(\rho)) \rangle_z$ at the high temperature excitation.

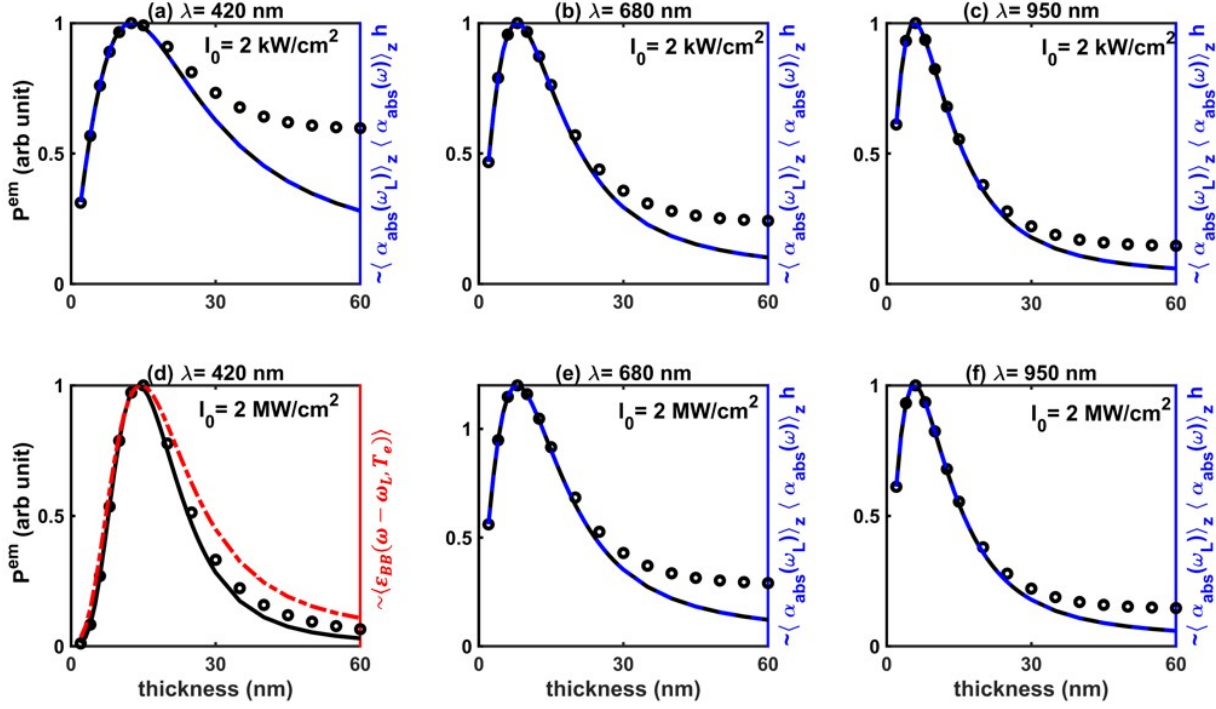


Figure 7: (Color online) The total PL calculated for the films using Eq. (9) (circles) and that using uniform field approximation (black continuous line) under CW illumination with $\lambda_L = 488$ nm and emission wavelengths of $\lambda = 420$ nm ((a) and (d)), $\lambda = 680$ nm ((b) and (e)) and $\lambda = 950$ nm ((c) and (f)). For these calculations, $p_{sat} \sim 1.2 \times 10^{25}$ W/m³ and I_0 values are (a)-(c) 2 kW/cm² and (d)-(f) 2 MW/cm². The dashed blue lines represent $\langle \alpha_{abs}(\omega_L) \rangle_z \langle \alpha_{abs}(\omega) \rangle_z h$ and the red dash-dot lines represent $\langle \mathcal{E}_{BB} \rangle$.

Note that unlike the case of spheres, the PL from the layer decreases monotonically beyond the increase for small sizes. The reason for that is the absence of the (high-order) resonances that occur for the spheres, into which the configuration is tuning in and out.

3.2.3 Comparison to experiments

As done above for single particles, we now compare the predictions of our simple analytic formula to recent experimental measurements. Specifically, we look at the data of Bowman *et al.*,⁷³ which presents the ratios of PL measurements from single crystal Au layers of various thicknesses to that of the thickest layers. Only a few layer thicknesses were studied, but data is available for several emission frequencies (rather than for single frequencies, as for

spheres).

The normalized PL spectra presented in Fig. 3(c) and Fig. S20(b) from Bowman *et al.*²⁸ are reproduced in Fig. 8(a) and (c) and Fig. 8(b) and (d), respectively, along with our own theory of PL of films (Eq. (9)). Our calculations closely match the experimental and theoretical results of Bowman *et al.*,²⁸ for all thicknesses studied (see results for the thicker films $h = 47$ nm and 79 nm in Fig. 17). There are, however, small discrepancies observed for thinner films occurring at different parts of the spectra. In order to check whether they represent a quantum effect, as claimed in Ref. [28], the PL is also calculated by modifying the Drude damping constant Γ to $\Gamma + A\frac{v_F}{h}$, where v_F is the Fermi velocity and A is the proportionality factor that can range from 0.1 to 2.⁶⁹ We show that the choice $A = 0.1$ yields an improved match for the excitation at 785 nm, but for the PL calculated for excitation at 488 nm it actually causes a deviation from the experimental data.

In light of this overall good agreement, it is notable that our simple theory deviates only slightly from the sophisticated quantum mechanical calculations which were highlighted in the original work;²⁸ indeed, the theory in that study involved the summation of the individual dipole emissions, a treatment of the electron states as a discrete set in momentum space, and a detailed DFT-based calculation of the permittivity. Those we replaced by the local Kirchhoff Law, empiric permittivity data, and our simple analytic formula for PL (Eq. (9)) based on a continuous set of energy states, along with standard macroscopic electromagnetic and thermal calculations. In that sense, beside the inconclusive role of the quantum size effect, the only quantum aspect of our theory is the use of the quantum version of the Boltzmann equation (see Ref. [39]), while the electron states themselves (and thus, the permittivity) nor the photon properties do not involve quantization. In fact, our theoretical predictions match the more sophisticated theory of Ref. [28] even where the latter does not match the experimental data well.

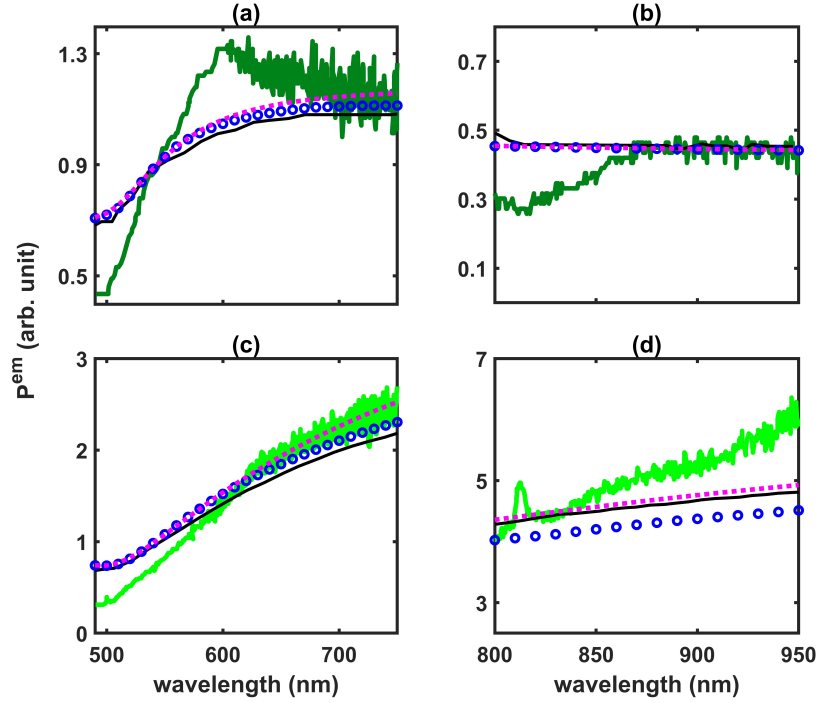


Figure 8: (Color online) The experimental (colored solid lines) and simulation (black solid lines) results for the PL from golds layers of thickness (a)-(b) $h = 33.3$ nm and (c)-(d) $h = 13.4$ nm, taken from Fig. 3(c) and Fig. S20(b) of Bowman *et al.*²⁸ In these calculations, the PL is integrated over a solid angle with the emission angle ranging from 0 to 44° corresponding to the numerical aperture of the objective lens used in the experiment. They are compared to our calculation (Eq. (9)) shown as blue circles. Panels (a) and (c) show the ratio $\frac{PL(h)}{PL(h=113\text{nm})}$ as a function of emission wavelength, using excitation conditions of $\lambda_L = 488$ nm, $I_{in} = 0.162\text{mW}/\mu\text{m}^2$ and Panels (b) and (d) display the normalized difference $\frac{PL(h)-PL(h=88\text{nm})}{PL(h=25.8\text{nm})-PL(h=88\text{nm})}$ at $\lambda_L = 785$ nm with $I_{in} = 1.87\text{mW}/\mu\text{m}^2$. Calculations including quantum size effects are represented by the magenta dotted lines.

4 Discussion

In this work, we provide a unifying explanation for the dependence of the PL from metal nanostructures on their size. Specifically, using the experimentally-established expression for the non-equilibrium electron distribution in the conduction band,^{39,40,42-44} together with recent extension of the local Kirchhoff Law for light emission from metals characterized this non-equilibrium electron distribution,³⁶ we provide a simple analytical form for the (intensity, temperature and) size-dependence of the PL. In particular, we show that the size-dependence of the Stokes emission (SE) is determined primarily by the size-dependence of the absorption (= emission) cross-section density (aka emissivity density) but that the aSE is much more sensitive to the structure size at high illumination intensities due to the exponential dependence of the Bose function $\langle \mathcal{E}_{BB}(\omega, T_e) \rangle$ on the electron temperature T_e .

In particular, our predictions imply that, generically, the PL from spheres and layers grows for small sizes as the volume / thickness, respectively, and then decreases due to the decrease of the average local field (or equivalently, of the emissivity). The size for which maximal PL is attained is found to be larger for spheres than for layers (e.g., ~ 30 nm vs. ~ 10 nm, respectively, for illumination near resonance; the maximal size grows for off-resonant illumination). This explains the seemingly contradicting trends observed (e.g., Ref. [16,23,24]) - an increase of the PL from spheres of growing size, and a decrease of the PL from layers of growing thickness. Specifically, our analysis shows that the different size-dependence of the PL reported in experiments originates from the fact that measurements from thin films^{16,28} were so far performed only for layers thicker than the size of maximal PL (> 10 nm), most likely, because films of such thickness tends to be discontinuous (below the percolation limit). A similar behaviour was observed for rods.

Our predictions were shown to match well a range of experimental results of SE, including for cases that formally lie beyond the limits of validity of the analysis, including non-spherical particles and their arrays. The quantitative discrepancies observed in some

cases may originate in differences in the underlying permittivity data, in subtleties associated with the significant field non-uniformity in this case, or in missing elements needed for a complete description of the PL, e.g., the inclusion of emission originating from inelastic electron scattering, which was already shown to dominate the emission near the pump frequency.³² Even better understanding of these discrepancies may be obtained by comparing to aSE measurements, which were so far done in the context of thermometry,^{5–8} but not done systematically as a function of the size.

Our analytic approach provides an easily accessible alternative to the highly complicated rigorous (discrete k -space) calculations of the PL offered in some recent studies.^{28,29,32} In particular, the use of the extension of the local Kirchhoff Law to non-equilibrium electron distributions³⁶ allows circumventing many of the detailed electromagnetic emission calculations done in Ref. [28] and validates approximations made, e.g., the neglect of the energy-dependence of the matrix elements and electron density of states; this finding is in line with good agreement obtained when matching our theoretical approach to measurement of currents in molecular and current junctions.^{41–44} Moreover, while the analytic expression we provide accounts for both intraband and interband absorption events (via the empiric values of the permittivity), unlike the rigorous approaches mentioned, our approach accounts only for emission events occurring within the conduction band. Nevertheless, our predictions are found to be in good agreements with experimental data from Au nanostructures in regimes for which interband emission was shown to be significant. This implies that interband emission events have primarily a quantitative effect on the PL, but not a qualitative one.

Nevertheless, while both rigorous k -space approach and our approximate analytic approaches are capable of reproducing most aspects of the experimental observations, the current study highlights the ability of the more rigorous approaches to capture subtle aspects such as the determination of the conditions under which the emission is due to radiative recombination or inelastic scattering (see, e.g., discussions in Ref. [4,28,32,74–78]), and identify the mechanism underlying the high sensitivity of the PL to the number of atomic levels

observed in Ref. [16].

While in the current work we focused on the PL from simple structures and noble metals, our approach can be applied also to more complicated structures for which the local electric field is even more non-uniform such as long rods,⁷⁹ various particle dimers,^{32,79–81} trimers⁸² etc., or to other plasmonic materials, including low electron density Drude materials such as transparent conducting oxides.^{83,84}

We also emphasize that the analysis in the current manuscript is limited to CW illumination, but could be extended also to pulsed illumination.^{9,10,16,20,85} In this scenario, which was studied more extensively in the past, the size-dependence of the temperature is different, and there is a dynamic transition between the non-thermal and thermal parts (see Ref. [34]), which entails further complexity. This class of experiments will be analyzed separately in future work.

Ultimately, our work paves the way to simple optimization of the PL for practical purposes.

Acknowledgements. I. K. and Y.S. were partially funded by Israel Science Foundation (ISF) grant no. 340/2020, a Lower-Saxony - Israel collaboration grant no. 76251-99-7/20 (ZN 3637) as well as a grant from the Bronitzki family.

A Appendix: Additional figures

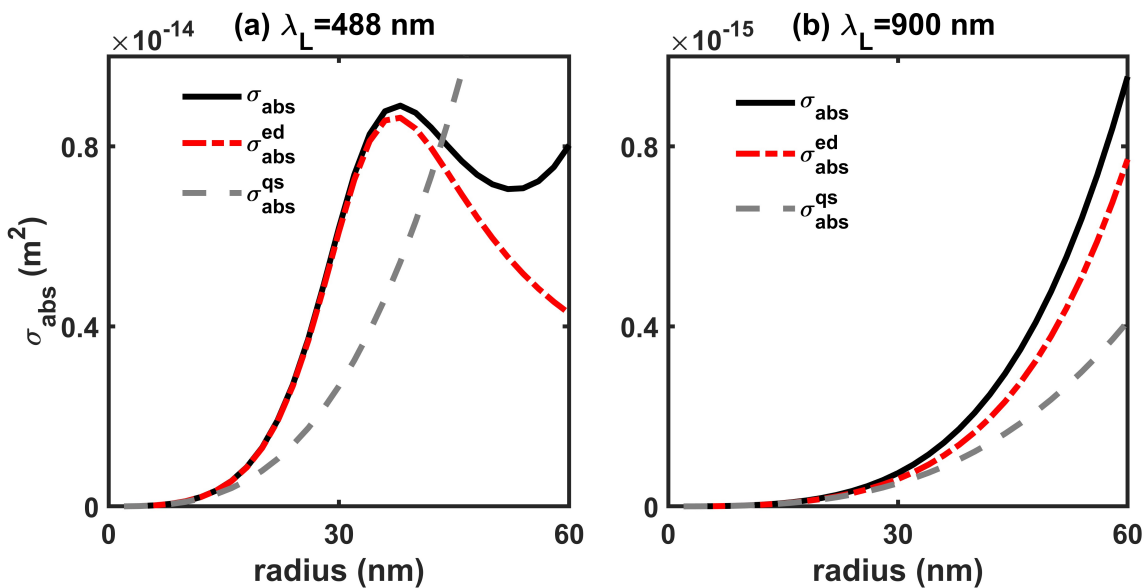


Figure 9: (Color online) The absorption cross-section (σ_{abs}),^{61?} the dipolar contribution to the absorption cross-section (σ_{abs}^{ed}) and the absorption cross section in the quasi-static limit (σ_{abs}^{qs})⁶¹ are calculated for Ag spheres in oil at the wavelengths (a) 488 nm and (b) 900 nm.

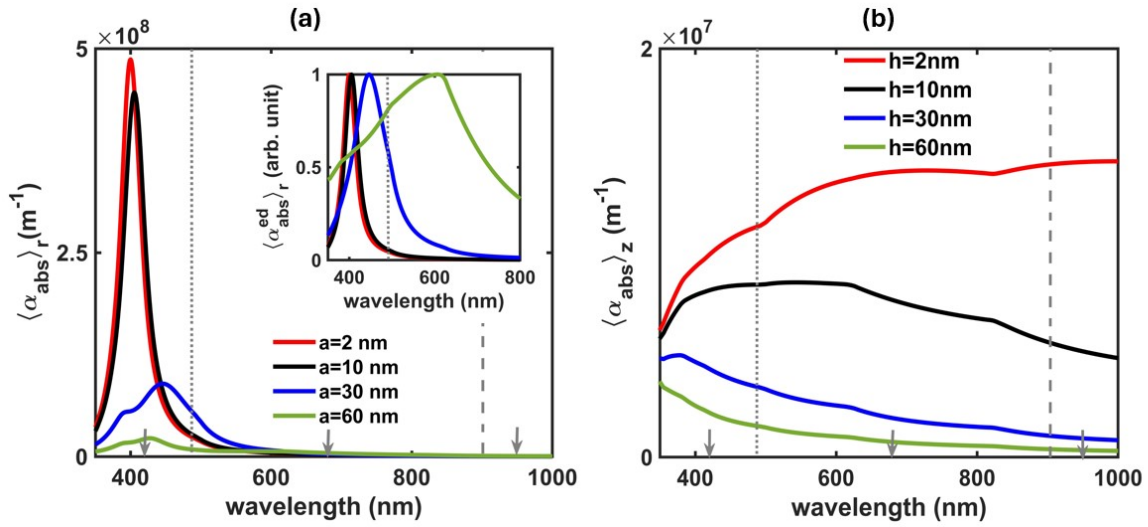


Figure 10: (Color online) (a) The spectral dependence of the volume-averaged absorption cross section density, $\langle \alpha_{abs}(\omega, \mathbf{r}) \rangle_r$, calculated for Ag nano-spheres of radius a ranging from 2 nm to 60 nm in oil. The contribution from the electric dipole mode alone, represented by $\langle \alpha_{abs}^{ed}(\omega, \mathbf{r}) \rangle_r = \sigma_{abs}^{ed}/V$, is shown in the inset. (b) The spectral dependence of $\langle \alpha_{abs}(\omega, \mathbf{r}) \rangle_z$ calculated for Ag films of thickness h varying from 2 nm to 60 nm. In both cases, dotted and Dashed gray vertical lines indicate the absorption wavelengths 488 nm and 900 nm, respectively, and the arrows indicate emission wavelengths 420 nm, 680 nm and 950 nm. Red, black, blue and green color indicates radii $a = 2, 10, 30$ and 60 nm, respectively, in (a) and thicknesses $h = 2, 10, 30$ and 60 nm, respectively in (b).

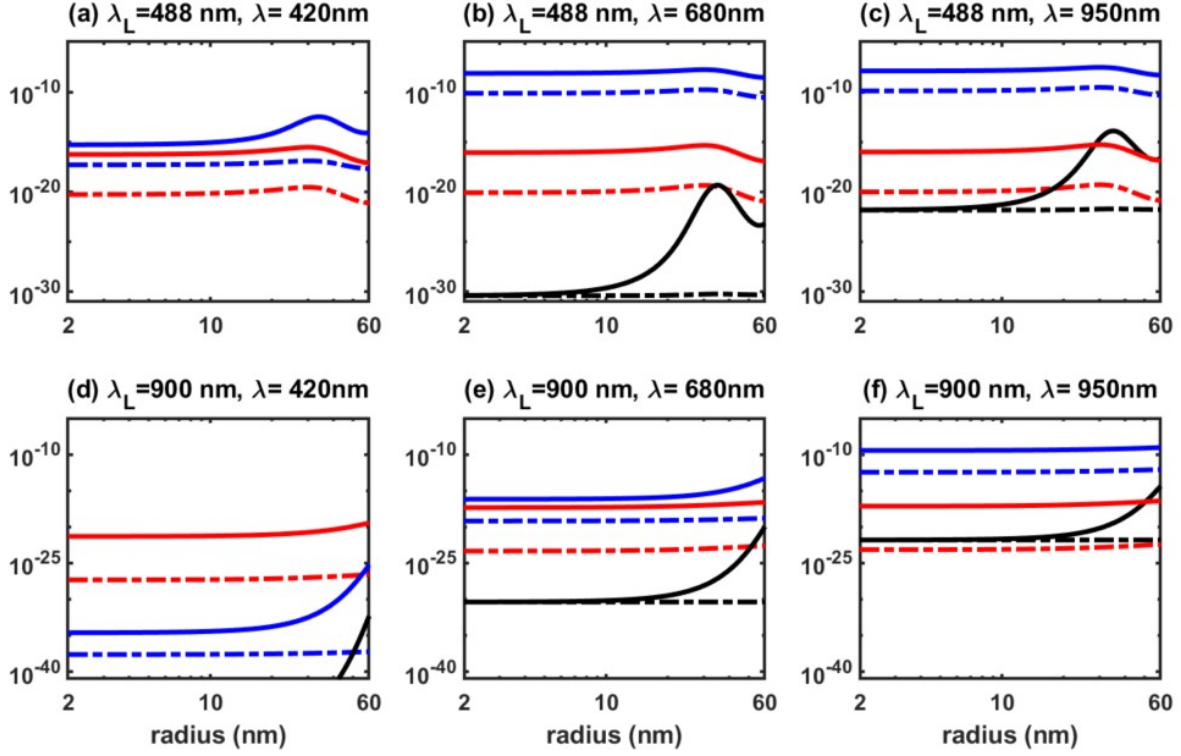


Figure 11: (Color online) The thermal and nonthermal contributions to I_e (i.e., the terms in Eq. (4)): $\langle \mathcal{E}_{BB}(\omega; T_e) \rangle$ (black), $2\langle \mathcal{E}_{BB}(\omega - \omega_L; T_e) \rangle \delta_E$ (blue), $\langle \mathcal{E}_{BB}(\omega - 2\omega_L; T_e) \rangle \delta_E^2$ (red) calculated for Ag spheres immersed in oil due to continuous wave illumination with (a)-(c) $\lambda_L = 488$ nm and (d)-(f) $\lambda_L = 900$ nm. Calculations are done at emission wavelengths $\lambda = 420$ nm ((a) and (d)), $\lambda = 680$ nm ((b) and (e)) and $\lambda = 950$ nm ((c) and (f)) corresponding to $I_{in} = 0.25$ MW/cm² (indicated by continuous line) and $I_{in} = 2.5$ kW/cm² (indicated by dash-dot line) for (a)-(c) and $I_{in} = 3.5$ MW/cm² (indicated by solid line) and $I_{in} = 3.5$ kW/cm² (indicated by dash-dot line) for (d)-(f). The thermal emission $\langle \mathcal{E}_{BB}(\omega; T_e) \rangle$ is notably low for aSE beyond the considered range, see (a) and (d).

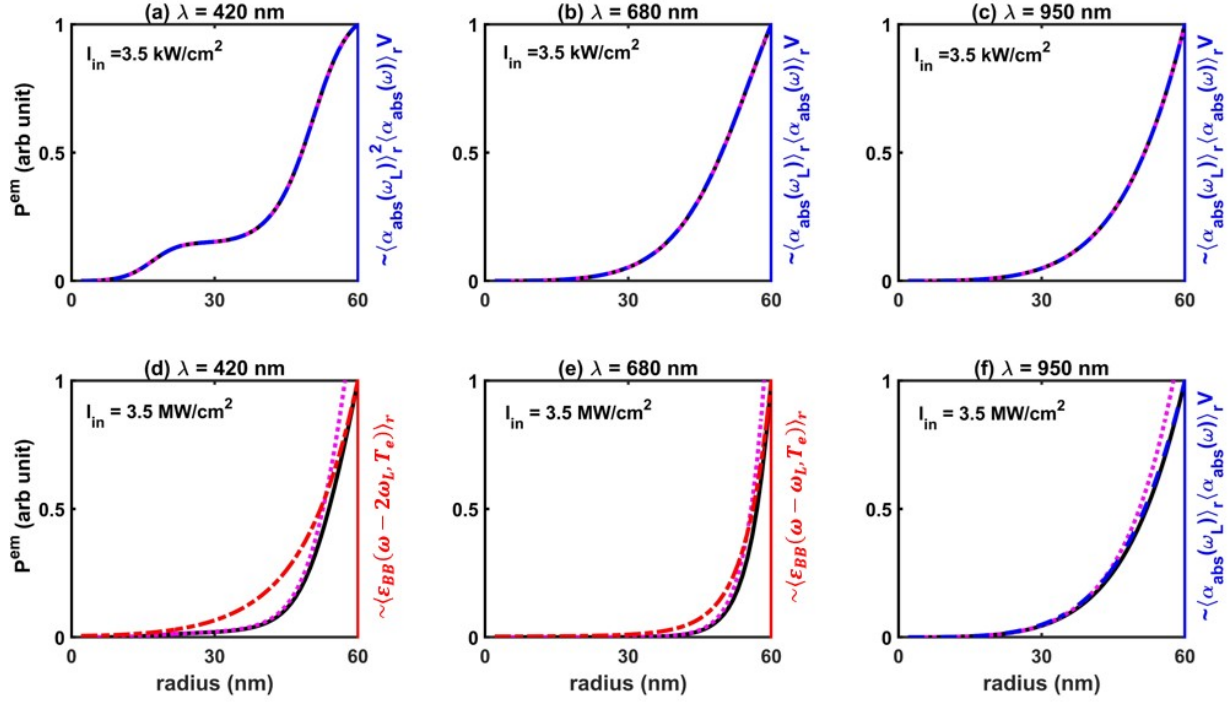


Figure 12: (Color online) The PL calculated for spheres using the homogenized approximation (Eq. (12); black solid line) under CW illumination, excited off-resonance at $\lambda_L = 900 \text{ nm}$, and emission wavelengths of $\lambda = 420 \text{ nm}$ ((a) and (d)), $\lambda = 680 \text{ nm}$ ((b) and (e)) and $\lambda = 950 \text{ nm}$ ((c) and (f)). For these calculations, $p_{sat} \sim 1.0 \times 10^{23} \text{ W/m}^3$ and the incident intensity, I_{in} used for the calculation are (a)-(c) 3.5 kW/cm^2 and (d)-(f) 3.5 MW/cm^2 . The dashed blue lines represent $V\langle\alpha_{abs}(\lambda_L)\rangle_r\langle\alpha_{abs}(\lambda)\rangle_r$, and the red dash-dot lines represent $\langle\mathcal{E}_{BB}\rangle_r$. The magenta dotted line shows the PL calculation (Eq. (12)) when the thermo-optic effect is included. Frequency and wavelength are used interchangeably, as convenient.

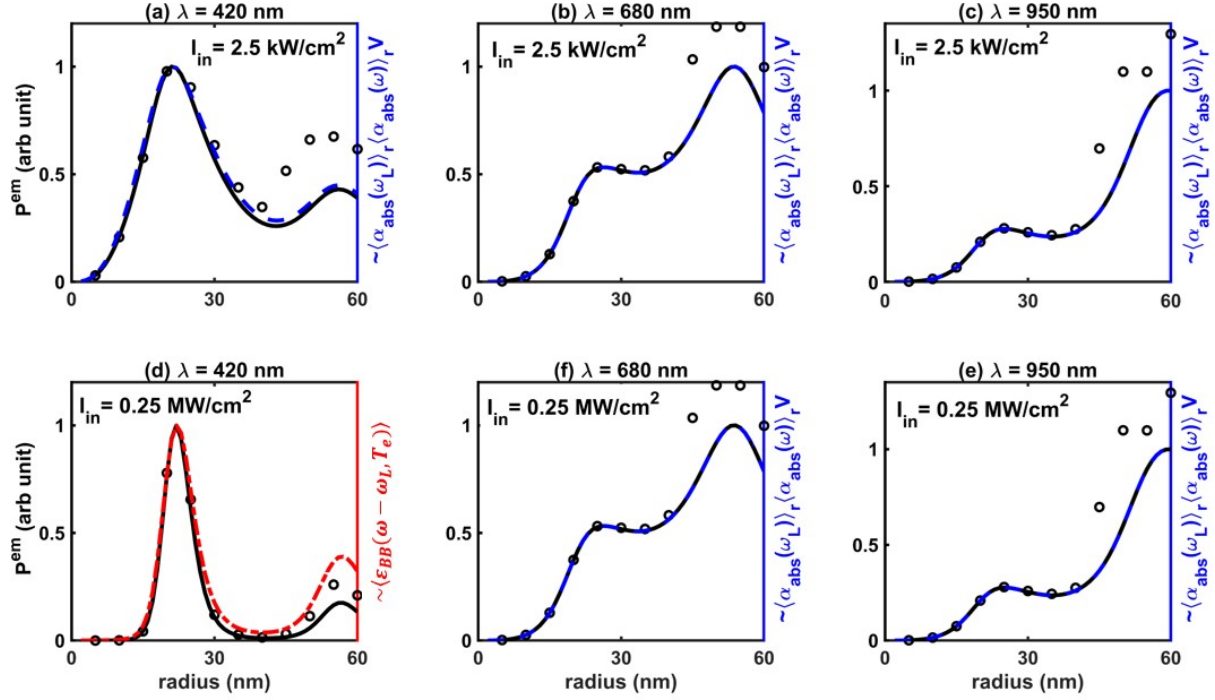


Figure 13: (Color online) The total PL (Eq. (9); circles) and its homogenized approximation (Eq. (12); black continuous line) calculated for spheres for background refractive index 1.8, under CW illumination at $\lambda_L = 488$ nm and emission wavelengths of $\lambda = 420$ nm ((a) and (d)), $\lambda = 680$ nm ((b) and (e)), and $\lambda = 950$ nm ((c) and (f)). I_{in} used for the calculation are (a)-(c) 2.5 kW/cm^2 and (d)-(f) 0.25 MW/cm^2 . The dashed blue lines represent $a^3 \langle \alpha_{abs}(\lambda_L) \rangle_r \langle \alpha_{abs}(\lambda) \rangle_r$ and the red dash-dot lines represent $\langle \mathcal{E}_{BB} \rangle$. Frequency and wavelength are used interchangeably, as convenient.

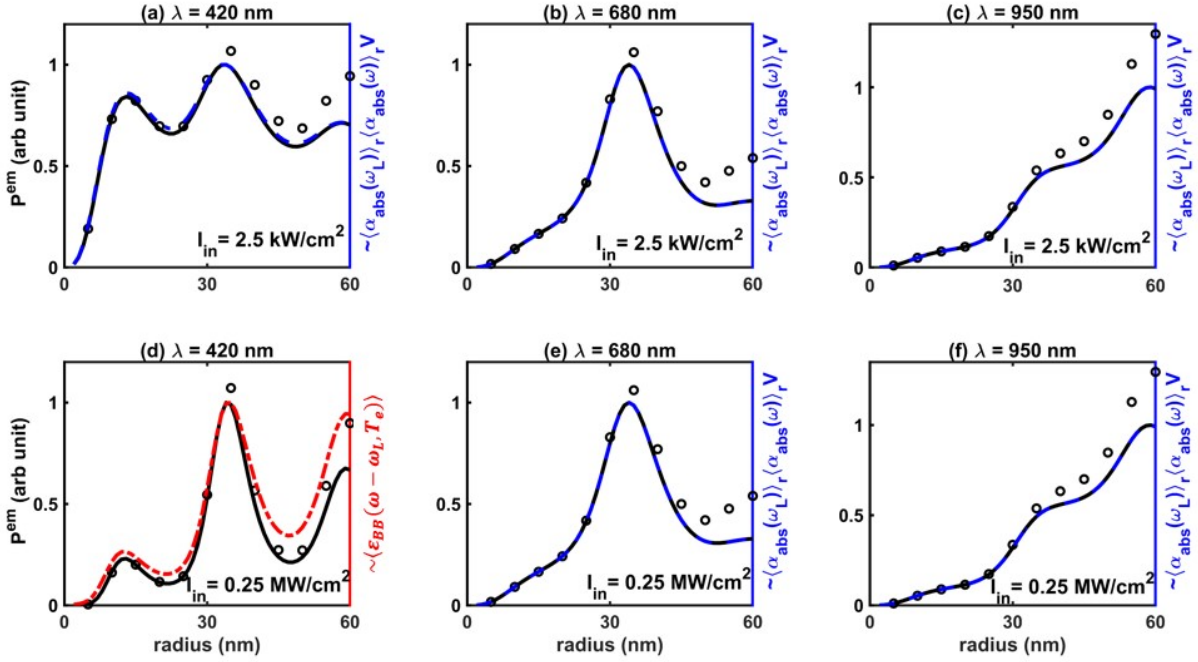


Figure 14: (Color online) Same as Fig. 13 for background refractive index 2.2.

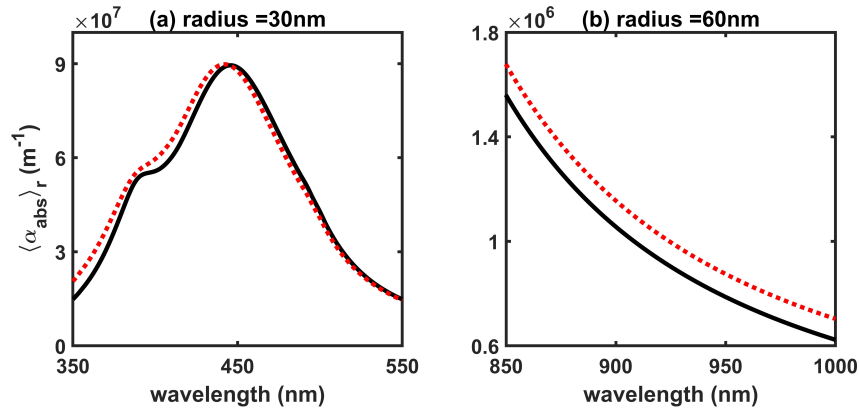


Figure 15: (Color online) $\langle \alpha_{abs} \rangle_r$ calculated for Ag nano-spheres of radius (a) $a = 30$ nm, (b) $a = 60$ nm, immersed in oil at room temperature (black solid line) and at $450^\circ K$ (red dotted line).

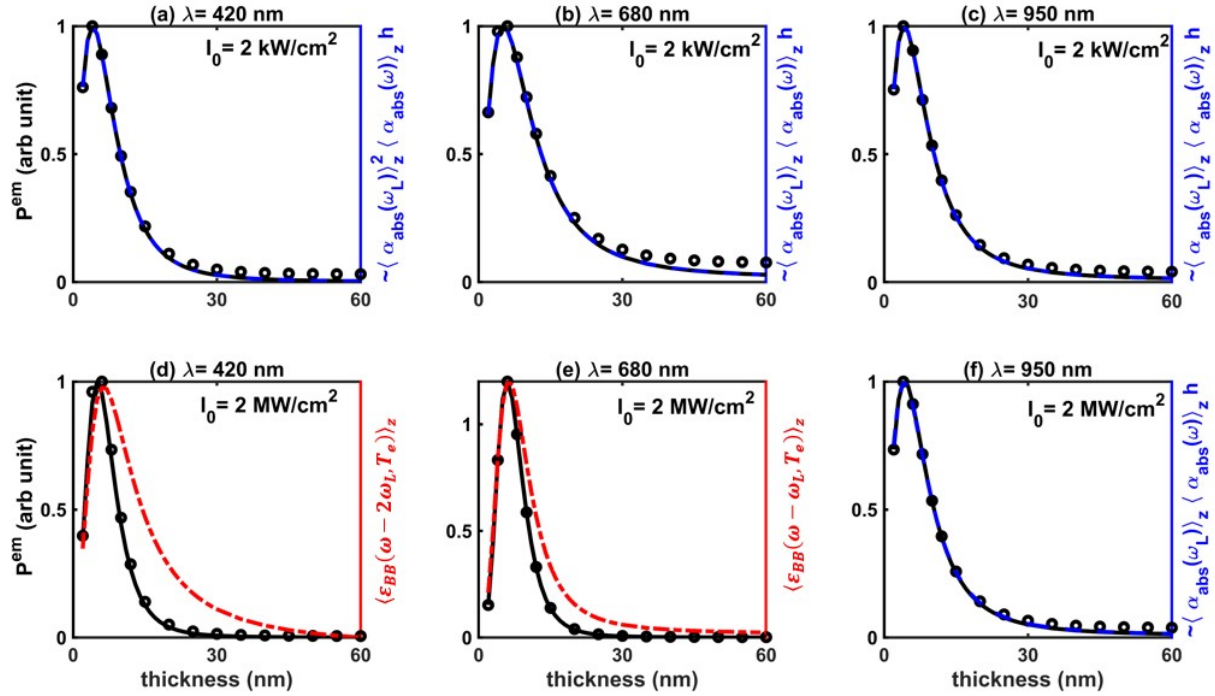


Figure 16: (Color online) The total PL calculated for the films using Eq. (9) (circles) and that using uniform field approximation (black continuous line) under CW illumination at $\lambda_L = 900$ nm and emission wavelengths of $\lambda = 420$ nm ((a) and (d)), $\lambda = 680$ nm ((b) and (e)) and $\lambda = 950$ nm ((c) and (f)). I_0 values are (a)-(c) 2 kW/cm^2 and (d)-(f) 2 MW/cm^2 . The dashed blue lines represent $\langle \alpha_{abs}(\omega_L) \rangle_z \langle \alpha_{abs}(\omega) \rangle_z h$ and the red dash-dot lines represent $\langle \mathcal{E}_{BB} \rangle$.

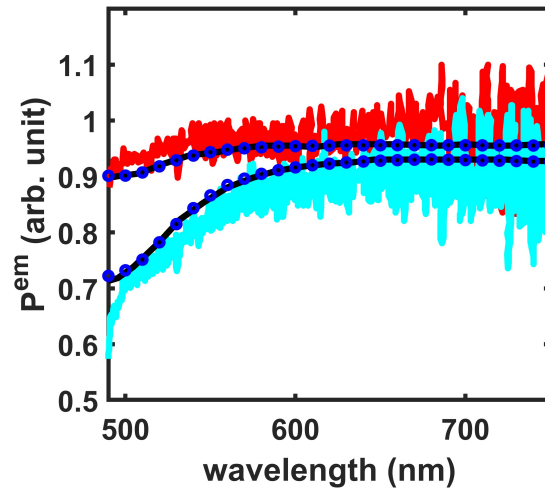


Figure 17: (Color online) The experimental results for the PL from gold layers, for thicknesses $h = 47$ nm (sky blue solid line) and $h = 79$ nm (red solid line) and the corresponding simulations (black solid lines) taken from,[?] showing the ratio $\frac{PL(h)}{PL(h=113\text{nm})}$ as a function of emission wavelength for the excitation conditions of $\lambda_L = 488$ nm, $I_{in} = 0.162\text{mW}/\mu\text{m}^2$. The corresponding calculations using (Eq. (9)) are shown as blue circles.

References

- (1) Jain, P. K.; Lee, K. S.; El-Sayed, I. H.; El-Sayed, M. A. Calculated Absorption and Scattering Properties of Gold Nanoparticles of Different Size, Shape, and Composition: Applications in Biological Imaging and Biomedicine. *J. Phys. Chem. B* **2006**, *110*, 7238–7248.
- (2) Anker, J. N.; Hall, W. P.; Lyandres, O.; Shah, N. C.; Zhao, J.; van Duyne, R. P. Biosensing with plasmonic nanosensors. *Nat. Mater.* **2008**, *7*, 442–453.
- (3) Perkovic, M.; Kunz, M.; Endesfelder, U.; Bunse, S.; Wigge, C.; Yu, Z.; Hodorin, V. V.; Scheffer, M. P.; Seybert, A.; Malkusch, S.; Schuman, E. M.; Heilemann, M.; Frangakis, A. S. Correlative Light- and Electron Microscopy with chemical tags. *J. Struct. Bio.* **2014**, *186*, 205 – 213.
- (4) Hugall, J. T.; Baumberg, J. J. Demonstrating Photoluminescence from Au is Electronic Inelastic Light Scattering of a Plasmonic Metal: The Origin of SERS Backgrounds. *Nano Lett.* **2015**, *15*, 2600–2604.
- (5) Xie, X.; Cahill, D. G. Thermometry of Plasmonic Nanostructures by Anti-Stokes Electronic Raman Scattering. *Appl. Phys. Lett.* **2016**, *109*, 183104.
- (6) Carattino, A.; Caldarola, M.; Orrit, M. Gold Nanoparticles as Absolute Nano-Thermometers. *Nano Lett.* **2018**, *18*, 874–880.
- (7) Jones, S.; André, D.; Karpinski, P.; Käll, M. Photothermal Heating of Plasmonic Nanoantennas: Influence on Trapped Particle Dynamics and Colloid Distribution. *ACS Photonics* **2018**, *5*, 2878–2887.
- (8) Jollans, T.; Caldarola, M.; Sivan, Y.; Orrit, M. Effective Electron Temperature Measurement Using Time-Resolved Anti-Stokes Photoluminescence. *J. Phys. Chem. A* **2020**, *124*, 6968–6976.

- (9) Beversluis, M.; Bouhelier, A.; Novotny, L. Continuum Generation from Single Gold Nanostructures through Near-Field Mediated Intraband Transitions. *Phys. Rev. B* **2003**, *68*, 115433.
- (10) Roloff, L.; Klemm, P.; Gronwald, I.; Huber, R.; Lupton, J. M.; Bange, S. Light Emission from Gold Nanoparticles under Ultrafast Near-Infrared Excitation: Thermal Radiation, Inelastic Light Scattering, or Multiphoton Luminescence? *Nano Lett.* **2017**, *17*, 7914–7919.
- (11) Sivan, Y.; Dubi, Y. Theory of “Hot” Photoluminescence from Drude Metals. *ACS Nano* **2021**, *15*, 8724–8732.
- (12) Mooradian, A. Photoluminescence of Metals. *Phys. Rev. Lett.* **1969**, *22*, 185.
- (13) Boyd, G. T.; Yu, Z. H.; Shen, Y. R. Photoinduced Luminescence from the Noble Metals and Its Enhancement on Roughened Surfaces. *Phys. Rev. B* **1986**, *33*, 7923.
- (14) Ghenuche, P.; Cherukulappurath, S.; Taminiau, T. H.; van Hulst, N. F.; Quidant, R. Spectroscopic Mode Mapping of Resonant Plasmon Nanoantennas. *Phys. Rev. Lett.* **2008**, *101*, 116805.
- (15) Shahbazyan, T. V. Theory of Plasmon-Enhanced Metal Photoluminescence. *Nano Lett.* **2013**, *13*, 194–198.
- (16) Grossmann, S.; Friedrich, D.; Karolak, M.; Kullock, R.; Krauss, E.; Emmerling, M.; Sangiovanni, G.; Hecht, B. Nonclassical Optical Properties of Mesoscopic Gold. *Phys. Rev. Lett.* **2019**, *122*, 246802.
- (17) Lee, A.; Wu, S.; Yim, J. E.; Zhao, B.; Sheldon, M. T. Hot Electrons in a Steady State: Interband vs. Intraband Excitation of Plasmonic Gold. *ACS Nano* **2024**, *18*, 19077–19085.

- (18) Cai, Y.-Y.; Sung, E.; Zhang, R.; Tauzin, L. J.; Liu, J. G.; Ostovar, B.; Zhang, Y.; Chang, W.-S.; Nordlander, P.; Link, S. Anti-Stokes Emission from Hot Carriers in Gold Nanorods. *Nano Lett.* **2019**, *19*, 1067–1073.
- (19) Huang, J.; Wang, W.; Murphy, C. J.; Cahill, D. G. Resonant Secondary Light Emission from Plasmonic Au Nanostructures at High Electron Temperatures Created by Pulsed-Laser Excitation. *Proc. Nat. Acad. Sci. U.S.A* **2014**, *111*, 906–911.
- (20) Haug, T.; Klemm, P.; Bange, S.; Lupton, J. M. Hot-Electron Intraband Luminescence from Single Hot Spots in Noble-Metal Nanoparticle Films. *Phys. Rev. Lett.* **2015**, *115*, 067403.
- (21) Liu, J. G.; Zhang, H.; Link, S.; Nordlander, P. Relaxation of Plasmon-Induced Hot Carriers. *ACS Photonics* **2018**, *5*, 2584–2595.
- (22) Ai, Q.; Zhang, H.; Wang, J.; Giessen, H. Multiphoton Photoluminescence in Hybrid Plasmon-Fiber Cavities with Au and Au@Pd Nanobipyramids: Two-Photon vs. Four-Photon Processes and Rapid Quenching. *ACS Photonics* **2021**, *8*, 2088.
- (23) Dulkeith, E.; Niedereichholz, T.; Klar, T. A.; Feldmann, J.; von Plessen, G.; Gittins, D. I.; Mayya, K. S.; Caruso, F. Plasmon Emission in Photoexcited Gold Nanoparticles. *Phys. Rev. B* **2004**, *70*, 205424.
- (24) Gaiduk, A.; Yorulmaz, M.; Orrit, M. Correlated absorption and photoluminescence of single gold nanoparticles. *Chem. Phys. Chem.* **2011**, *12*, 1536–1541.
- (25) Hu, H.; Duan, H.; Yang, J. K. W.; Shen, Z. X. Plasmon-Modulated Photoluminescence of Individual Gold Nanostructures. *ACS Nano* **2012**, *6*, 10147–10155.
- (26) Zheng, J.; Zhou, C.; Yu, M.; Liu, J. Different sized luminescent gold nanoparticles. *Nanoscale* **2012**, *4*, 4073.

- (27) Lin, K.-Q.; Yi, J.; Hu, S.; Sun, J.-J.; Zheng, J.-T.; Wang, X.; Ren, B. Intraband Hot-Electron Photoluminescence from Single Silver Nanorods. *ACS Photonics* **2016**, *3*, 1248–1255.
- (28) Bowman, A. R.; Echarri, A. R.; Kiani, F.; Iyikanat, F.; Tsoulos, T. V.; Cox, J. D.; Sundararaman, R.; de Abajo, F. J. G.; Tagliabue, G. Quantum-mechanical effects in photoluminescence from thin crystalline gold films. *Light: Science and Applications* **2024**, *13*, 91.
- (29) Echarri, A. R.; Iyikanat, F.; Boroviks, S.; Mortensen, N. A.; Cox, J. D.; de Abajo, F. J. G. Nonlinear photoluminescence in gold thin films. *ACS Photonics* **2023**, *10*, 2918–2929.
- (30) Brown, A. M.; Sundararaman, R.; Narang, P.; Goddard, W. A.; Atwater, H. A. Nonradiative Plasmon Decay and Hot Carrier Dynamics: Effects of Phonons, Surfaces, and Geometry. *ACS Nano* **2016**, *10*, 957–966.
- (31) Lee, S. A.; Kuhs, C. T.; Searles, E. K.; Everitt, H. O.; Landes, C. F.; Link, S. d-Band Hole Dynamics in Gold Nanoparticles Measured with Time-Resolved Emission Upconversion Microscopy. *Nano Lett.* **2023**, *23*, 3501–3506.
- (32) Amoruso, A. B.; Boto, R. A.; Elliot, E.; de Nijs, B.; Esteban, R.; Földes, T.; Aguilar-Galindo, F.; Rosta, E.; Aizpurua, J.; Baumberg, J. J. Uncovering low-frequency vibrations in surface-enhanced Raman of organic molecules. *Nature Comm.* **2024**, *15*, 6733.
- (33) Koopman, W.; Stete, F.; Bargheer, M. Auger-excited Photoluminescence from Gold Nanoflowers. *ChemRxiv* **2024**, <https://chemrxiv.org/engage/chemrxiv/article-details/66a0b2b05101a2ffa8d10e89>.
- (34) Sivan, Y.; Un, I. W.; Kalyan, I.; Lin, K.; Lupton, J.; Bange, S. Crossover from non-

- thermal to thermal photoluminescence from metals excited by ultrashort light pulses. *ACS Nano* **2023**, *17*, 11439–11453.
- (35) Un, I. W.; Sivan, Y. Size-dependence of the Photothermal Response of a Single Metal Nanosphere. *J. Appl. Phys.* **2019**, *126*, 173103.
- (36) Loirette-Pelous, A.; Greffet, J.-J. Theory of photoluminescence by metallic structures. *ACS Nano* **2024**, *18*, 31823–31833.
- (37) Sivan, Y.; Chu, S.-W. Nonlinear Plasmonics at High Temperatures. *Nanophotonics* **2017**, *6*, 317–328.
- (38) Gurwich, I.; Sivan, Y. A Metal Nanosphere under Intense Continuous Wave Illumination - a Unique Case of Non-Perturbative Nonlinear Nanophotonics. *Phys. Rev. E* **2017**, *96*, 012212.
- (39) Dubi, Y.; Sivan, Y. “Hot” Electrons in Metallic Nanostructures - Non-Thermal Carriers or Heating? *Light: Sci. Appl.* **2019**, *8*, 89.
- (40) Sivan, Y.; Un, I. W.; Dubi, Y. Assistance of Plasmonic Nanostructures to Photocatalysis - Just a Regular Heat Source. *Faraday Discuss.* **2019**, *214*, 215–233.
- (41) Reddy, H.; Wang, K.; Kudyshev, Z.; Zhu, L.; Yan, S.; Vezzoli, A.; Higgins, S. J.; Gavini, V.; Boltasseva, A.; Reddy, P.; Shalaev, V. M.; Meyhofer, E. Determining plasmonic hot-carrier energy distributions via single-molecule transport measurements. *Science* **2020**, *369*, 423–426.
- (42) Dubi, Y.; Un, I. W.; Sivan, Y. Distinguishing thermal from non-thermal (“hot”) carriers in illuminated molecular junctions. *Nano Letters* **2022**, *5*, 2127–2133.
- (43) Février, P.; Basset, J.; Estéve, J.; Aprili, M.; Gabelli, J. Role of optical rectification in photon-assisted tunneling current. *Communications Physics* **2023**, *6*, 29.

- (44) Lin, C.; Krecinic, F.; Yoshino, H.; Hammud, A.; Pan, A.; Wolf, M.; Müller, M.; Kumagai, T. Continuous-Wave Multiphoton-Induced Electron Transfer in Tunnel Junctions Driven by Intense Plasmonic Fields. *ACS Photonics* **2023**, *10*, 3637–3646.
- (45) Greffet, J.-J.; Bouchon, P.; Brucoli, G.; Marquier, F. Light Emission by Nonequilibrium Bodies: Local Kirchhoff Law. *Phys. Rev. X* **2018**, *8*, 021008.
- (46) Bailly, E.; Chevrier, K.; de la Vega, C. R. P.; Hugonin, J.-P.; Wilde, Y. D.; Krachmalnicoff, V.; Vest, B.; Greffet, J.-J. Method to measure the refractive index for photoluminescence modelling. *Optical Materials Express* **2022**, *12*, 2772–2781.
- (47) Nguyen, A.; Greffet, J.-J. Efficiency optimization of mid-infrared incandescent sources with time-varying temperature. *Optical Materials Express* **2022**, *12*, 225–239.
- (48) Reif, F. *Fundamentals of statistical and thermal physics*; McGraw-Hill Science/Engineering/Math, 1965.
- (49) Fatti, N. D.; Voisin, C.; Achermann, M.; Tzortzakis, S.; Christofilos, D.; Valleé, F. Nonequilibrium electron dynamics in noble metals. *Phys. Rev. B* **2000**, *61*, 16956–16966.
- (50) Saavedra, J. R. M.; Asenjo-García, A.; de Abajo, F. J. G. Hot-Electron Dynamics and Thermalization in Small Metallic Nanoparticles. *ACS Photonics* **2016**, *3*, 1637–1646.
- (51) Baffou, G.; Quidant, R. Thermo-plasmonics: Using metallic nanostructures as nano-sources of heat. *Laser Photon. Rev.* **2013**, *7*, 171–187.
- (52) Block, A.; Liebel, M.; Yu, R.; Spector, M.; Sivan, Y.; de Abajo, J. G.; van Hulst, N. F. Tracking ultrafast hot-electron diffusion in space and time by ultrafast thermomodulation microscopy. *Science Advances* **2019**, *5*, eaav8965.
- (53) Sivan, Y.; Spector, M. Ultrafast dynamics of optically heat gratings in metals. *ACS Photonics* **2020**, *7*, 1271–1279.

- (54) Gao, G.; Jiang, L.; Xue, B.; Yang, F.; Wang, T.; Wan, Y.; Zhu, T. Unconventional Shrinkage of Hot Electron Distribution in Metal Directly Visualized by Ultrafast Imaging. *Small Methods* **2023**, 2201260.
- (55) Block, A.; Yu, R.; Un, I. W.; Varghese, S.; Liebel, M.; van Hulst, N. F.; Fan, S.; Tielrooij, K. Y.; Sivan, Y. Observation of negative effective thermal diffusion in gold films. *ACS Photonics* **2023**, *10*, 1150–1158.
- (56) Karna, P.; Hoque, M. S. B.; Thakur, S.; Hopkins, P. E.; Giri, A. Direct Measurement of Ballistic and diffusive Electron Transport in Gold. *Nano Lett.* **2023**, *23*, 491–496.
- (57) Bernardi, M.; Mustafa, J.; Neaton, J. B.; Louie, S. G. Theory and computation of hot carriers generated by surface plasmon polaritons in noble metals. *Nat. Commun.* **2015**, *6*, 7044.
- (58) Sivan, Y.; Un, I. W.; Sarkar, S. Ballistic vs. diffusive transport in metals. <https://arxiv.org/pdf/2402.15226> **2024**,
- (59) Meng, L.; Yu, R.; Qiu, M.; de Abajo, F. J. G. Plasmonic Nano-Oven by Concatenation of Multishell Photothermal Enhancement. *ACS Nano* **2019**, *11*, 7915–7924.
- (60) Baffou, G.; Quidant, R.; de Abajo, F. J. G. Nanoscale Control of Optical Heating in Complex Plasmonic Systems. *ACS Nano* **2010**, *4*, 709–716.
- (61) Bohren, C. F.; Huffman, D. R. *Absorption and scattering of light by small particles*; Wiley & Sons, 1983.
- (62) Un, I. W.; Sivan, Y. The Thermo-Optic Nonlinearity of Single Metal Nanoparticles under Intense Continuous-Wave Illumination. *Phys. Rev. Mater.* **2020**, *4*, 105201.
- (63) Boyd, R. W. *Nonlinear Optics*, 2nd ed.; Academic Press, San Diego, 2003.

- (64) Lee, H.; Im, S.; Lee, C.; Lee, H.; Chu, S.-W.; Ho-Pui, A.; Kim, H. D. Probing Temperature-Induced Plasmonic Nonlinearity: Unveiling Opto-Thermal Effects on Light Absorption and Near-Field Enhancement. *Nano Letters* **2024**, *6*, 3598–3605.
- (65) Reddy, H.; Guler, U.; Chaudhuri, K.; Dutta, A.; Kildishev, A. V.; Shalaev, V. M.; Boltasseva, A. Temperature-Dependent Optical Properties of Single Crystalline and Polycrystalline Silver Thin Films. *ACS Photonics* **2017**, *4*, 1083–1091.
- (66) Shen, P.-T.; Sivan, Y.; Lin, C.-W.; Liu, H.-L.; Chang, C.-W.; Chu, S.-W. Temperature- and -roughness dependent permittivity of annealed/unannealed gold films. *Opt. Exp.* **2016**, *24*, 19254.
- (67) Reddy, H.; Guler, U.; Kildishev, A. V.; Boltasseva, A.; Shalaev, V. M. Temperature-dependent optical properties of gold thin films. *Optical Materials Express* **2016**, *6*, 2776–2802.
- (68) Kreibig, U.; Vollmer, M. *Optical Properties of Metal Clusters*; Springer: Berlin, 1995.
- (69) Alvarez, M. M.; Khoury, J. T.; Schaaff, T. G.; Shafigullin, M. N.; Vezmar, I.; Whetten, R. L. Optical Absorption Spectra of Nanocrystal Gold Molecules. *J. Phys. Chem.* **1997**, *101*, 3706–3712.
- (70) Johnson, P. B.; Christy, R. W. Optical constants of noble metals. *Phys. Rev. B* **1972**, *6*, 4370–4379.
- (71) Aspnes, D. E.; Studna, A. A. Dielectric functions and optical parameters of Si, Ge, GaP, GaAs, GaSb, InP, InAs, and InSb from 1.5 to 6.0 eV. *Phys. Rev. B* **1983**, *27*, 985–1009.
- (72) Ohta, K.; Ishida, H. Matrix formalism for calculation of electric field intensity of light in stratified multilayered films. *Applied Optics* **1990**, *29*, 1952–1959.
- (73) Ref. 28, Fig. 3(b) and Fig. S20(b).

- (74) Shen, Y. R. Distinction between Resonant Raman Scattering and Hot Luminescence. *Phys. Rev. B* **1974**, *9*, 622–626.
- (75) Klein, M. V. Equivalence of Resonance Raman Scattering in Solids with Absorption Followed by Luminescence. *Phys. Rev. B* **1973**, *8*, 919–921.
- (76) Solin, J. R.; Merkelo, H. Resonant Scattering or Absorption followed by Emission. *Phys. Rev. B* **1975**, *12*, 624–629.
- (77) Solin, J. R.; Merkelo, H. Reply to “Comment on ‘Resonant Scattering or Absorption Followed by Emission’”. *Phys. Rev. B* **1976**, *14*, 1775–1776.
- (78) Shen, Y. R. Comment on “Resonant Scattering or Absorption Followed by Emission”. *Phys. Rev. B* **1976**, *9*, 1772–1774.
- (79) Agreda, A.; Sharma, D. K.; Viarbitskaya, S.; Hernandez, R.; Cluzel, B.; Demichel, O.; Weeber, J.-C.; des Francs, G. C.; Kumar, G.; Bouhelier, A. Spatial Distribution of the Nonlinear Photoluminescence in Au Nanowires. *ACS Photonics* **2019**, *6*, 1240–1247.
- (80) Huang, D.; Byers, C. P.; Wang, L.-Y.; Hoggard, A.; Hoener, B.; Dominguez-Medina, S.; Chen, S.; Chang, W.-S.; Landes, C. F.; Link, S. Photoluminescence of a Plasmonic Molecule. *ACS Nano* **2015**, *9*, 7072–7079.
- (81) Lemasters, R.; Manjare, M.; Freeman, R.; Wang, F.; Pierce, L. G.; Hua, G.; Urazhdin, S.; Harutyunyan, H. Non-thermal emission in gap-mode plasmon photoluminescence. *Nature Communications* **2024**, *10*, 4468.
- (82) Yin, T.; Dong, Z.; Jiang, L.; Zhang, L.; Hu, H.; Qiu, C.-W.; Yang, J. K. W.; Shen, Z. X. Anomalous Shift Behaviors in the Photoluminescence of Dolmen-Like Plasmonic Nanostructures. *ACS Photonics* **2016**, *3*, 979–984.
- (83) Kinsey, N.; DeVault, C.; Boltasseva, A.; Shalaev, V. M. Near-zero-index materials for photonics. *Nat. Rev. Mater.* **2019**, *4*, 742–760.

- (84) Un, I. W.; Sarkar, S.; Sivan, Y. An electronic-based model of the optical nonlinearity of low electron density Drude materials. *Phys. Rev. Applied* **2023**, *19*, 044043.
- (85) Suemoto, T.; Yamanaka, K.; Sugimoto, N. Observation of femtosecond infrared luminescence in gold. *Phys. Rev. B* **2019**, *100*, 125405.